A&A, 710, A69 (2026)
https://doi.org/10.1051/0004-6361/202558444

Astronomy & Astrophysics

ExoplaNeT accRetion mOnitoring sPectroscopic surveY (ENTROPY)

III. Optical He I line profiles of the accreting super Jupiter Delorme 1 (AB)b

Gayathri Viswanath[1,2,⋆], Mickaël Bonnefoy[2], Catherine Dougados[2], Simon C. Ringqvist[1],
Markus Janson[1], Dorian Demars[3], Aurora Sicilia-Aguilar[4], Jérôme Bouvier[2],
Gabriel-Dominique Marleau[5,6,7], Evelyne Alecian[2], and Gaël Chauvin[8]

[1] Institutionen för astronomi, Stockholms universitet, AlbaNova universitetscentrum, 106 91 Stockholm, Sweden
[2] Université Grenoble Alpes, CNRS, IPAG, 38000 Grenoble, France
[3] Department of Astronomy, University of Virginia, 530 McCormick Rd, Charlottesville, VA 22904, USA
[4] SUPA, School of Science and Engineering, University of Dundee, Nethergate, DD1 4HN Dundee, UK
[5] Fakultät für Physik, Universität Duisburg–Essen, Lotharstraße 1, 47057 Duisburg, Germany
[6] Max-Planck-Institut für Astronomie, Königstuhl 17, 69117 Heidelberg, Germany
[7] Division of Space Research & Planetary Sciences, Physics Institute, University of Bern, Sidlerstr. 5, 3012 Bern, Switzerland
[8] Laboratoire Lagrange, Université Côte d'Azur, CNRS, Observatoire de la Côte d'Azur, 06304 Nice, France

Received 6 December 2025 / Accepted 9 March 2026

ABSTRACT

Context. Observations of helium emission lines from classical T Tauri stars at high resolution ($R_\lambda > 10\,000$) offer great potential, showing distinct profile characteristics that help probe regions within the accretion geometry untapped by hydrogen lines. Parallel studies in the planetary-mass regime have not been explored.

Aims. We investigate helium line emission from the nearby (47 pc), wide orbit (∼84 au), ∼13 $M_{\rm Jup}$, accreting circumbinary companion Delorme 1 (AB)b and analyse the resolved profile characteristics to infer clues to line origin.

Methods. We obtained high signal-to-noise spectra of the target over 33 exposures with VLT/UVES over near-ultraviolet to optical wavelengths at high resolution ($R_\lambda \sim 50\,000$). We studied the helium line profiles in the spectra and compared them to helium emission recorded from both accreting and non-accreting young stellar objects.

Results. We detected seven neutral helium (He I) lines $\lambda\lambda 3890, 4027, 4473, 4923, 5017, 5877, 6680$ at high confidence ($> 5\sigma$), with notable flux variation between epochs. The line profiles of He I $\lambda\lambda 5877, 4923, 4473, 4027$ show clear asymmetry, with a narrow component at ∼0 km s^{-1} and a broad component redshifted by ∼15 km s^{-1}. The accretion luminosity ($1.3^{+1.6}_{-0.7} \times 10^{-5}\ L_\odot$) and mass accretion rate ($0.7^{+0.9}_{-0.4} \times 10^{-8}\ M_{\rm Jup}\ {\rm yr}^{-1}$) obtained from median He I line luminosities using empirical scaling relations from stars are comparable but slightly higher than from the target's ultraviolet excess emission.

Conclusions. The protoplanet Delorme 1 (AB)b exhibits asymmetric He I lines similar to classical T Tauri stars, but with much smaller widths for the narrow and broad components. The triplet–singlet line ratio, a strong correlation with ultraviolet excess and the near-zero, redshifted velocities obtained for the narrow component suggest that it originates within the post-shock region, close to the planet surface. The persistent redshift of the broad component, its line width, and velocity correlation with the narrow component imply an origin within the shock structure, closer to the shock front. Emission seems to be dominated by accretion based on the obtained accretion luminosities, but a contribution from chromospheric activity may be present.

Key words. accretion, accretion disks – techniques: spectroscopic – planets and satellites: formation – planets and satellites: individual: Delorme 1 (AB)b

1. Introduction

Decades of observations of classical T Tauri stars (CTTS) have provided a rich database to study the interplay between young, low-mass stars and the accretion disks that feed their formation. A wealth of accretion signatures have been recorded and studied from these class of objects; a few prominent ones include infrared excess from the accretion disk, ultraviolet (UV) excess emission from the accretion shock on the stellar surface, subsequent strong Hα and higher order Balmer line emission, both neutral (He I) and ionised helium (He II) emission as well as Ca II emission. A forest of metallic emission lines from species such as Fe, Ca, Na, and Ti has also been detected, including forbidden lines that trace outflows and jets from the accretion process (see Hartmann et al. 2016). These observations have led to the consensus that in young, accreting, solar-type stars, material from the inner disk is fed to the star along magnetic field lines of a strong magnetosphere; this is the so-called magnetospheric accretion paradigm. Analysing the emission line profiles from this phenomenon at high resolution ($R_\lambda > 10\,000$) has helped uncover details of the geometry of magnetospheric accretion as well as the physical conditions within these regions.

In comparison, the parallel in the planetary-mass regime has been much less explored owing largely to the faintness of

---

[⋆] Corresponding author: `gayathri.viswanath@astro.su.se` the phenomenon. Early observations with seeing-limited echelle spectrograph revealed a diversity of profiles in brown dwarfs down to ∼15 $M_{\rm Jup}$ (Jayawardhana et al. 2003; Mohanty et al. 2003, 2005; Muzerolle et al. 2005). More recent observations have begun to exploit the accretion signatures of planetary mass objects (PMOs; < 15 $M_{\rm Jup}$) but have been mostly limited to hydrogen line emission and conducted at modest resolution (R_λ < 10 000) (e.g. Boucher et al. 2016; Santamaría-Miranda et al. 2018, 2019; Haffert et al. 2019; Chinchilla et al. 2021; Eriksson et al. 2020; Betti et al. 2022; Demars et al. 2023; Aoyama et al. 2024; Almendros-Abad et al. 2025; Currie et al. 2025). Attempts to predict the physical origin of these emission lines have been made with various accretion models (e.g. Aoyama et al. 2018; Thanathibodee et al. 2019; Szulágyi & Ercolano 2020; Aoyama et al. 2024; Hashimoto & Aoyama 2025). Compared to H I, helium lines have a much higher excitation potential, requiring high temperatures or close proximity to an ionizing source, and thus serve a stricter confinement of the region of line origin. Resolved helium line profiles catalogued in CTTS (e.g. Ulrich & Wood 1981; Muzerolle et al. 1998; Beristain et al. 2001; Edwards 2003; Edwards et al. 2006; Erkal et al. 2022) show both broad and narrow components, as well as absorption features, attributed to composite line origins that are difficult to probe with hydrogen lines (Kwan et al. 2007; Kwan 2024); prominent narrow components (NC) from accretion shock at the stellar surface, absorption features from inner winds and prominent broad components (BC) whose origin, although determined to be non-shock, is yet unclear. However, high-resolution observations of helium emission from PMOs have not been reported, except in one case (Viswanath et al. 2024), despite He I λ5877 being a prevalent accretion signature in the higher-mass regime (>20 $M_{\rm Jup}$).

Located 47 ± 3 pc away in the Tucana–Horologium stellar association, Delorme 1 (AB)b is a wide-orbit (∼84 au) ∼13 $M_{\rm Jup}$ companion to an M5.5-type binary system (Delorme et al. 2013). Eriksson et al. (2020) reported strong Hα emission from this planetary-mass companion (PMC; <15$M_{\rm Jup}$) with the Multi Unit Spectroscopic Explorer (MUSE; Bacon et al. 2010) at the Very Large Telescope (VLT) in Chile, followed by detections of Paβ, Paγ, and Brγ emission in the near-infrared (NIR) by Betti et al. (2022). Recent observations by Mâlin et al. (2025) with the *James Webb* Space Telescope's Mid-Infrared Instrument (JWST/MIRI; Wells et al. 2015) confirmed the presence of warm gas in a circumplanetary disk (CPD) around the object, with indications of outflows and an inner disk cavity. These evidences show that this object is actively accreting despite its relatively old age of ∼40 Myr. Having a mass at the deuterium-burning limit, its nearby distance and wide orbital separation (1.8″) offer a convenient opportunity to study up close the accretion at a PMC using high-resolution spectroscopy.

Previous observations in October 2021 with the Ultraviolet and Visual Echelle Spectrograph (UVES; Dekker et al. 2000) at VLT, at a high resolution of R_λ ∼ 50 000, revealed resolved spectral lines of higher-order Balmer transitions H5 to H9 (Ringqvist et al. 2023) from the target, with complex line profiles consisting of both broad and narrow components similar to CTTS. Recently, follow-up observations were conducted with VLT/UVES, spanning multiple epochs, as part of the ExoplaNeT accRetion mOnitoring sPectroscopic surveY (ENTROPY) program. ENTROPY aims to understand the accretion process in planetary-mass objects (<20 $M_{\rm Jup}$) using high-resolution spectroscopic techniques (Viswanath et al. 2024; Demars et al. 2026). The second paper of this series (Demars et al. 2026; hereafter ENTROPY II) presented a detailed analysis of the hydrogen emission lines in Delorme 1 (AB)b and their variability based on these observations. The complex Balmer line profiles obtained from the target's spectra were decomposed into two static components: a narrow 'core' component, centred at ∼0 km s^{-1}, and a broad 'wings' component at ∼−50 km s^{-1} with an absorption feature at ∼15 km s^{-1}. While the wings component is reproduced best by modelling emission from accretion columns, the core component is consistent with both predictions from shock emission models and chromospheric activity. The overall line profiles show strong variability of ∼100% on average on a time scale of weeks.

Our work here presents the helium emission lines in the same spectra, providing the first focused report on helium lines at high resolution from an accreting PMC. The analysis combines the recently acquired data with the target's observations from 25 October 2021 (Ringqvist et al. 2023) taken with VLT/UVES with the same set-up. The paper is organised as follows. Section 2 provides a summary of the observations and reduction routines employed to get the final spectrum used for the analysis in this work. The main results from the identified lines are outlined in Section 3. Section 4 provides a detailed analysis of the characteristics of the lines, and its implications are discussed in Section 5, while Section 6 summarises the key conclusions of this work.

2. Observations and data reduction

Delorme 1 (AB)b was observed with VLT/UVES between 13 October 2022 and 2 January 2023 as part of ENTROPY. The observations covered near-UV to optical wavelengths (3300–6800 Å) at a resolution of R_λ ∼ 50 000. The integration time was 1482 s, providing the same observing set-up as the 2021 epoch (Ringqvist et al. 2023) for Delorme 1 (AB)b. Including the two previous epochs on 25 October 2021, the new observations yielded 33 exposures over 11 nights. The total on-source integration time is 13.6 h, yielding a high S/N for the emission lines detected in the median spectrum.

Data were reduced using the ESO/UVES data handling pipeline (Ballester et al. 2000) and the extraction of the primary and companion spectra was performed using a custom CLEAN-like procedure (Högbom 1974) outlined in detail in ENTROPY II. The companion spectra were flux calibrated based on the spectrophotometric calibration of the primary spectra using its *Gaia* DR3 (Gaia Collaboration 2023) G_{BP} magnitude (15.690±0.005). The resulting companion spectra were then corrected for the target's radial velocity (7.3±2.6 km/s; Kraus et al. 2014). After correcting for barycentric motion, a grand median was obtained over all 33 exposures which offered high S/N for the emission lines in the spectrum, optimal for their identification. Additionally, individual exposures from each night of observation were combined to yield a median spectrum per night, which allowed for assessing epoch-to-epoch flux variation in the emission lines identified from the grand median.

We used the python package STAR-MELT[1] (Campbell-White et al. 2021) to identify emission lines in the spectra, with a tolerance velocity shift of ±8 km s^{-1} (∼3σ of the target's radial velocity) around the rest wavelengths. We also fit the line profiles using STAR-MELT and defined the S/N of the identified lines based on the peak of the Gaussian fit to its profile and the standard deviation within ±150 km s^{-1} around the central wavelength. STAR-MELT has been extensively used for analysing CTTS emission spectra (e.g.

---

[1] `https://github.com/justyncw/STAR_MELT`

Table 1. Characteristics of He I emission lines detected in this work.

$\lambda_{\rm rest,\,vac}$ (Å)	E_k (eV)	Transition[a]	A_{ki}[b] (10^6 s^{-1})	Fit[c]	$\lambda_{\rm obs,\,vac}$ (Å)	FWHM (km s^{-1})	Velocity (km s^{-1})	Flux (10^{-17} erg s^{-1} cm^{-2})	S/N (σ)
3889.75	23.01	T 3p–2s	9.5	s	3889.75	7.2 ± 0.8	−0.2 ± 0.3	3.0 ± 3.6	6
4027.33	24.04	T 5d–2p	4.8	s	4027.40	23.5 ± 1.0	5.4 ± 0.3	7.9 ± 2.5	9
				d, NC	4027.33	13.0 ± 2.2	0.1 ± 0.6	8.3 ± 2.5	10
				d, BC	4027.45	26.4 ± 1.7	9.2 ± 1.6		
4472.73	23.74	T 4d–2p	24.6	s	4472.78	20.1 ± 0.5	3.7 ± 0.2	19.5 ± 3.2	18
				d, NC	4472.74	14.4 ± 2.4	0.3 ± 1.1	20.9 ± 3.2	20
				d, BC	4472.89	22.0 ± 6.3	10.4 ± 7.0		
4923.31	23.74	S 4d–2p	19.9	s	4923.36	16.2 ± 0.4	2.9 ± 0.2	6.1 ± 1.6	13
				d, NC	4923.34	11.8 ± 0.5	1.9 ± 0.2	7.5 ± 1.6	14
				d, BC	4923.47	33.3 ± 2.1	9.8 ± 1.2		
5017.08	23.09	S 3p–2s	13.4	s	5017.10	13.4 ± 0.3	0.9 ± 0.1	6.5 ± 1.7	20
5877.25	23.07	T 3d–2p	53.0	s	5877.32	23.5 ± 0.3	3.7 ± 0.2	61.6 ± 1.5	132
				d, NC	5877.25	16.0 ± 0.2	−0.2 ± 0.1	68.4 ± 1.5	147
				d, BC	5877.56	23.4 ± 0.6	16.0 ± 0.5		
6679.99	23.07	S 3d–2p	63.7	s	6680.03	17.4 ± 0.1	1.5 ± 0.0	28.6 ± 1.8	77

Notes. [a]Triplet ($S = 1$) and singlet ($S = 0$) line transitions of He I, denoted respectively by T and S, are identified from Del Zanna et al. (2020). [b]A_{ki} denotes the Einstein coefficient for the transition. [c]s refers to a single Gaussian fit and d refers to a double Gaussian fit. Line characteristics for the narrow and broad components for the latter are indicated as NC and BC respectively.

Arulanantham et al. 2023; Campbell-White et al. 2023b,a; Sicilia-Aguilar et al. 2023). For details on the data reduction procedure, the observing log, and the final spectra over the full range of wavelength, we refer the reader to ENTROPY II.

3. Results

ENTROPY II showed that the Balmer emission lines in the reduced UVES spectra of Delorme 1 (AB)b display high flux variability (~100% on average) over time scales of weeks to months. These Balmer line profiles and the corresponding epochs can be classified into three classes depending on the observed shape of the Hα profile, namely ‘A’, ‘B’, and ‘C’ (see Fig. A.1). Class A profiles exhibit low flux levels as seen on 1, 4, and 5 November 2022, as well as the 2021 epoch. Class B profiles have profile shapes similar to those of Class A but with visibly higher flux intensities, pointing to higher mass accretion rates during these epochs. Class C profiles stand out from those of Class A and B due to the presence of an enhanced blue wing emission during the nights of 14, 15, and 17 October 2022, which could possibly trace an accretion burst or a chromospheric activity burst (see ENTROPY II). At wavelengths less than ~3700 Å, there is substantial UV continuum excess in the spectra, likely originating from accretion shock at the surface of the PMC. The spectra also present a nearly flat continuum throughout the wavelength range, with a gradual increase beyond ~5300 Å, which becomes more prominent during Class A epochs (see Fig. A.2). Using STAR-MELT, the continuum was fit using a standard Savitzky–Golay polynomial smoothing filter (see Campbell-White et al. 2021; Temmink et al. 2024; Mâlin et al. 2025) within every 12 Å wavelength window, with a first-order polynomial. All reported emission lines here were identified from the grand median spectrum after subtracting the above-fit continuum. The line list for line identification was taken from the NIST Atomic Database[2] and all wavelengths reported here are in vacuum.

3.1. Helium emission from Delorme 1 (AB)b

We report seven resolved optical helium emission lines from Delorme 1 (AB)b. Using the grand median over all epochs, we confirm, with high confidence, the tentative He I $\lambda\lambda$3890, 4027, 4473 emission lines reported in Ringqvist et al. (2023) from the 2021 epoch. In addition, we also detect four strong He I emission lines $\lambda\lambda$4923, 5017, 5877, and 6680 in the grand median spectrum. No He II emission was detected in the spectra. The strongest He I emission in the spectra is the triplet line λ5877, followed by the singlet line λ6680, both of which are prevalent in CTTS spectra. Table 1 lists the confirmed (>5σ) He I emission lines from the grand median spectra of Delorme 1 (AB)b and the characteristics of the corresponding line profiles. Since the major contribution to the flux uncertainty is from continuum subtraction, error bars on the integrated line flux values are estimated conservatively as the rms of the local continuum. Figure 1 illustrates the respective resolved line profiles in the grand median spectra and their least-χ^2 Gaussian fits.

The upper energy levels (E_k) of the detected He I line transitions are between 23–24 eV, with a maximum E_k of 24.04 eV for the line transition at 4027.33 Å. The He I transition at 3820.70 Å (E_k = 24.21 eV) is tentatively detected in emission at an S/N of 2σ (see Appendix B). For He I to be excited to such high energy levels of $\gtrsim 20$ *eV*, it requires either strong UV flux causing photoionisation, followed by recombination and cascade at lower temperatures of 8000–15 000 K, or collisional excitation resulting from high temperatures of 25 000–90 000 K in the emitting region (Beristain et al. 2001, hereafter BEK01). Section 5 provides further discussion of the origin of these He I lines from Delorme 1 (AB)b.

3.2. Asymmetry in the He I line profiles

He I λ5877 (He I D3) is one of the strongest and most prevalent permitted emission lines in CTTS optical spectra (BEK01). It is the strongest emission line in the Delorme 1 (AB)b spectra after the Balmer lines. The grand median profile of the line shows clear asymmetry in its red wing emission, with the

---

[2] `https://www.nist.gov/pml/atomic-spectra-database`

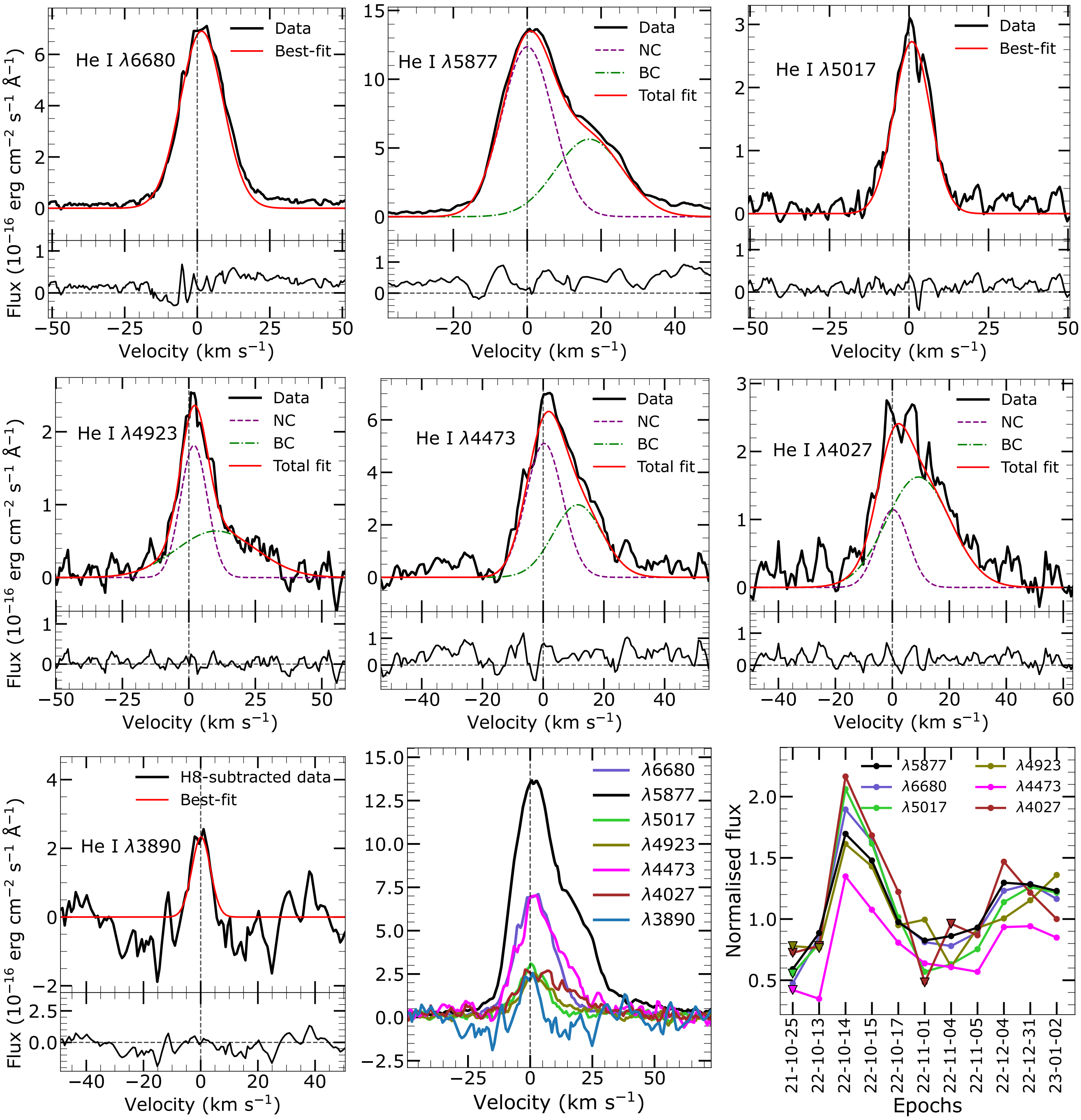

Fig. 1. Resolved profiles of He I emission lines (black) from Delorme 1 (AB)b detected from its grand median spectrum in this work. The red curve shows the least-χ^2 fit to the line profile, composed of either pure NC or with the addition of a BC. In case of the latter, the red curve represents the total profile fit. Residual from the fit is shown in the bottom sub-panel of each line plot. The line profile for $\lambda3890$ (bottom left) is obtained after the Balmer line H8 was modelled and subtracted from the data (see Appendix C). The bottom middle panel shows all the He I lines plotted against respective velocity scales, demonstrating relative strength and asymmetry. The bottom right panel illustrates the variability of their integrated line flux in time, normalised with respect to the corresponding grand median values. Downward triangles represent tentative detections with confidence between 1–3σ. The y-axis for all panels except the bottom right shows the flux in units of 10^{-16} erg cm^{-2} s^{-1} Å^{-1}.

least-χ^2 fit yielding two Gaussians (see Fig. 1, top middle panel), one centred at near-zero velocity with full width at half maximum (FWHM$_{\rm NC}$) 16.0 ± 0.2 km s^{-1}, and a second, broader component (FWHM$_{\rm BC}$ = 23.4 ± 0.6 km s^{-1}) redshifted by 16 km s^{-1}. Similar asymmetry in the red wing emission is also seen in the blue He I triplet lines $\lambda\lambda4473, 4027$, whose grand median profiles can also be decomposed into a narrow and broad component as shown in Fig. 1. These profiles show BCs with a slightly lower redshift (~10 km s^{-1}) than He I D3 but with an NC that remains at near-zero velocities.

The He I triplet lines are composed of two equal-intensity transitions at similar wavelengths and a third less intense transition separated by ~15 km s^{-1}. The second broader component in the χ^2−fit for He I $\lambda\lambda5877, 4473, 4027$ line profiles is centred very close to the respective third transition of these triplet lines, suggesting the possibility that the high resolution of the data could have partially de-blended the lines leading to the asymmetry. However, the BC/NC line ratio is much higher than expected from the ratio of relative intensities of the individual transitions listed in the NIST database. More importantly, the singlet line He I λ4923 also displays a similar asymmetry in its grand median profile, as illustrated in the first middle panel of Fig. 1. Its BC is redshifted similarly at ~10 km s^{-1}, but with a slightly broader profile (~33 km s^{-1}) than those of the triplet lines. A possible explanation for this asymmetry in the singlet line could be blending with an Fe II transition at 4923.56 Å, but the absence of any other Fe II line detections (>3σ) in the grand median spectrum renders this unlikely.

The singlet line He I λ6680 also displays a small but broad flux increase in its red wing (see the fit-residual in the first panel of Fig. 1), which can be subsequently fit with a very shallow BC at a redshift of ~15 km s^{-1}. However, the significantly lower intensity of the BC relative to the NC renders this fit tentative, so we only consider a single Gaussian fit to its profile for the line characteristics used in subsequent analysis. However, we note that the line profile is not very symmetric for He I λ6680, with more emission on the red side of the line centre than on the blue side, although not as pronounced as in He I D3. The velocity and FWHM of NCs and BCs of all the asymmetric He I lines in the grand median spectrum are listed in Table 1. The NC widths measured for all the asymmetric lines are broader than the spectral point spread function (PSF; 6 km s^{-1})[3] of UVES, which implies that these components are spectrally resolved by the instrument.

3.3. Time variability of the He I line profiles

All He I lines detected in this work demonstrate notable flux variation between individual epochs, similar to the Balmer lines shown in ENTROPY II. The bottom right panel of Fig. 1 illustrates the integrated flux of these He I emission lines (see Table E.1 for values) varying in a similar pattern within a time scale of days, offering clear indications of an accretion origin. Line emissions are strongest on 14 October. The flux of the strongest lines He I $\lambda\lambda$5877, 6680 varies by a factor of 3–4, similar to accretion signatures in CTTS. He I D3 remains asymmetric in all epochs (see Fig. E.2), with the intensities and widths of the respective NC and BC evolving in an increasing pattern from Class A to Class C epochs. While the centroid velocity of NC remains mostly within ±1 km s^{-1}, the velocity of BC is slightly more variable with time (see Fig. D.1 and Table E.2). The contribution of the BC to the total line strength also varies through the epochs; the line profile remains mostly NC-dominated but the BC/NC flux ratio varies from 0.31 (1 November 2022, Class A) to 0.76 (14 October 2022, Class C). The only exception is on 13 October 2022 when the He I D3 profile becomes BC-dominated with BC/NC flux ratio of 1.65 (see Fig. D.2). This epoch, which is right before the peak outburst on 14 October, stands out from the rest due to significantly lower UV excess emission in the spectrum, strong core Hα component, and strong He I D3 BC. In general, the relative BC contribution (i.e. the BC/NC flux ratio) in He I D3 line profile increases in the epochs of Class B and Class C compared to Class A (see Fig. D.1). This variation in the BC/NC flux ratio with time is another strong argument against the asymmetry in the line profiles originating from resolved triplet components.

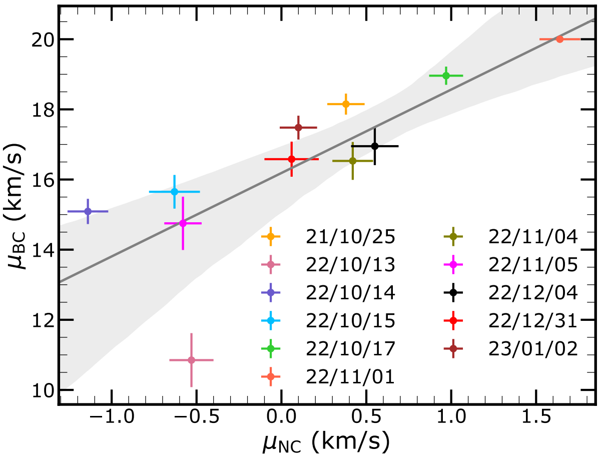

Fig. 2. Variation in the centroid velocity, μ, of NC and BC in He I D3 through the epochs. The grey line denotes the linear fit between NC and BC velocities, which are strongly correlated.

Compared to He I D3, the asymmetric He I lines at shorter wavelengths $\lambda\lambda$4923, 4473, 4027 are much lower in S/N. He I λ4473 is detected only at 2.6σ on 25 October 2021, and its profile is asymmetric in nine of the ten remaining epochs with S/N> 3σ. He I λ4923 remains asymmetric in eight of the nine epochs where its S/N is above 3σ. The emission at λ4027 is relatively weaker with the detection falling below 3σ in four of the nights, for which a two-component Gaussian fit was not warranted. The relative BC contributions in the He I λ4473 and λ4923 line profiles differ in their behaviour from that of He I D3, with both increasing on average in Class A epochs (see Fig. D.1) compared to Class C. For the relatively weaker λ4027 emission, the BC contribution is quite diverse, ranging from pure-NC profiles to nearly pure-BC profiles, but we refrain from a detailed analysis because the line is noisier.

3.4. Kinematics of NC and BC

The variation in the centroid velocity (μ) of NC and BC in He I D3 throughout the epochs is shown in Fig. 2 (see Table E.2 for the values). Its NC velocity seems to vary between positive and negative values over time, but remains mostly near-zero with a mean value of 0.1±0.8 km s^{-1}. The NC velocities of the lower S/N He I lines from the target also vary with time. The mean of these velocities from individual epochs is given in Table 2 for each of the detected He I lines of Delorme 1 (AB)b. The respective FWHM measurements are also given in the Table, with the width distribution relatively uniform among the NCs. In general, the mean NC velocities of these He I lines are slightly redshifted, in line with the origin in the immediate post-shock region at the base of the accretion column, as predicted in magnetospheric accretion scenarios (Hartmann et al. 2016, BEK01).

The centroid velocities of BC in He I D3 also varies in a pattern similar to that of its NC through the epochs. From Fig. 2, we see that the centroid velocities of the two components are strongly correlated in time with a Pearson's correlation coefficient, $r = 0.8$, at $p = 0.005$[4], which implies that NC and BC are likely formed via the same mechanism. The mean value of the BC velocities of individual epochs is given in Table 2 for He I D3

---

[3] https://www.eso.org/sci/facilities/paranal/instruments/uves/doc/ESO_514367_User_Manual_P115.pdf

[4] The p-value in the Pearson's correlation test indicates the statistical significance of the correlation, and the obtained correlation is considered not relevant if $p > 0.05$.

Table 2. Mean kinematics of He I lines, taken over individual fits from each epoch.

$\lambda_{\rm rest,\,vac}$ [a] (Å)	$\mu_{\rm NC}$ (km s^{-1})	FWHM$_{\rm NC}$ (km s^{-1})	$\mu_{\rm BC}$ (km s^{-1})	FWHM$_{\rm BC}$ (km s^{-1})
3880.75	0.5 ± 0.6	8 ± 2 [b]	–	–
4027.33	2.1 ± 3.8	15 ± 9	13.5 ± 6.5	27 ± 6
4472.73	1.6 ± 1.6	15 ± 4	15.0 ± 3.7	18 ± 8
4923.31	2.2 ± 0.5	14 ± 2	16.6 ± 5.0	30 ± 17
5017.08	0.6 ± 0.6	14 ± 1	–	–
5877.25	0.1 ± 0.8	16 ± 1	16.5 ± 2.3	21 ± 4
6679.99	1.4 ± 0.4	16 ± 1	–	–

Notes. [(a)] He I $\lambda\lambda$3890, 5017, 6680 lines are fit with a single Gaussian profile. [(b)] Line width of He I λ3890 emission is dependent on the efficiency of H8 modelling, and hence should be interpreted with caution.

and the other asymmetric He I lines. On average, the centroid velocities of BC in all asymmetric He I lines from the target seem redshifted with respect to NC, with the individual epochs having BC velocities ranging from ~10–22 km s^{-1}. The BC width distribution is more diverse between the He I lines than for NC, with mean values between 16–30 km s^{-1}. For the strongest line He I D3, the width of BC has a negative correlation in time with that of its NC ($r = -0.7$, $p = 0.02$; see Fig. D.2 right panel), resulting in the overall profile shape of the line being conserved over epochs.

4. Analysis

4.1. Comparison to He I emission in CTTS

4.1.1. Line profiles

BEK01 analysed He I profiles in the high-resolution ($R_\lambda \sim$ 20 000) spectra of 31 CTTS down to spectral type M5 using the KPNO 4 m telescope, detecting the He I lines $\lambda\lambda$4473, 5877, 6680 in several of the targets in their sample. Similarly to Delorme 1 (AB)b, the strongest He I emission in the sample was at He I D3, followed by He I λ6680. No He I emission was reported from the sample at $\lambda\lambda$3890, 4027, 4923, and 5017, while we detect these lines at high S/N from Delorme 1 (AB)b.

Among the He I D3 profiles in the BEK01 sample the morphology is quite diverse, ranging from BC-dominated profiles (flux ratio[5] BC/NC > 5) to NC-dominated profiles (BC/NC< 1). The composite He I D3 profile of Delorme 1 (AB)b remains NC-dominated in all epochs, except on 13 October 2022 (see Section 3.3). A similar asymmetry in the red wing, as seen in the He I emission lines in Delorme 1 (AB)b, was also displayed in the He I λ5877 and λ4473 emission line profiles of the M0.5 type TW Hya ($\dot{M}_{\rm acc} \approx 10^{-9}\ M_\odot$ yr^{-1}; see Herczeg et al. 2023).

The line profiles of He I λ6680 emission reported from the BEK01 sample also range from NC-dominated to BC-dominated profiles, while in Delorme 1 (AB)b the line is clearly NC-dominated, with only a tentative detection of a BC. BEK01 also reported composite profiles for the He I λ4473 emission, but excluded it from their analysis due to the suspected blending of the line with the strong BC in the Ti II emission at 208 km s^{-1}. For Delorme 1 (AB)b, the BC at ~13 km s^{-1} in He I λ4473 can be confirmed since at the higher resolution of the spectra, any blending from ~200 km s^{-1} can be confidently dismissed. Additionally, no Ti II lines are identified in the whole spectrum.

4.1.2. Kinematics of He I D3

In Fig. 3 we compare the NC and BC kinematics of the He I D3 profile in Delorme 1 (AB)b (filled data points) with those of the BEK01 CTTS sample[6] (unfilled data points). In the left panel, we see the centroid velocity distribution as a function of the mass of the accretor. For NC, the mean velocity (μ) for Delorme 1 (AB)b (see Table 2) is within the range of NC velocity distribution among CTTS ($\bar{\mu}_{\rm NC} = 5 \pm 4$ km s^{-1}), although slightly lower. The width distribution as a function of accretor mass (right panel) shows that NC is much narrower in Delorme 1 (AB)b than the typical NC width observed in CTTS (47±7 km s^{-1}).

Analysing the BC distribution of the BEK01 sample in Fig. 3, most of the observed BCs were found in blueshift, while also appearing redshifted in some sources; in fact, five of the sources in the BEK01 sample (DF Tau, DO Tau, DS Tau, UZ Tau E, and YY Ori) display only redshifted BC in all their observations. In CTTS when the magnetic dipole axis is inclined with respect to the stellar rotation axis (i.e. a non-axisymmetric alignment), the centroid velocity of BC may undergo a phase-dependent velocity modulation with time. Continued monitoring of CTTS emission lines has recorded such velocity shifts with time-resolved observations, including changes between redshift and blueshift (see Sicilia-Aguilar et al. 2023; Armeni et al. 2024). However, the centroid velocity of He I BC in Delorme 1 (AB)b is always redshifted, closely varying about ~ + 15 km s^{-1}, in our observations spanning days to months. This is within the range of the observed BC redshifts among the CTTS sample.

The width of BC in Delorme 1 (AB)b is not much wider than its NC, unlike what is seen among CTTS. The left panel of Fig. 3 clearly illustrates the very distinct width distribution of NC and BC among CTTS, while in Delorme 1 (AB)b this distinction is quite small, with the BC width much smaller than what is typically observed in CTTS (130–300 km s^{-1}); the BC-to-NC width ratio in the CTTS sample is always > 3, while for the target it is only 1.31±0.26. The redshifted and blueshifted BCs among CTTS are shown in separate colours (yellow and blue, respectively) in the figure, to highlight that ~90% of the blueshifted BCs have FWHM>200 km s^{-1}. On average, the redshifted BCs among CTTS have widths smaller than the blueshifted ones. A moderate positive correlation exists between mass and FWHM among the CTTS sample with a Pearson's correlation coefficient $r = 0.5$ (at $p \approx 10^{-3}$), suggesting that the BC width may be expected to be smaller at planetary masses. Delorme 1 (AB)b falls within the confidence interval of the linear fit between the BC width and mass of the CTTS sample, albeit larger than what is expected at its mass from the best-fit. This suggests that the smaller BC width for the target could be a consequence of the lower mass of the PMC.

A comparison with CTTS profiles can also be made for NC in the He I $\lambda\lambda$4473, 6680 lines. Similarly to λ5877, these lines also display narrower NCs at smaller redshifts compared to CTTS profiles in BEK01, with a mean FWHM ~37 km s^{-1} and a mean velocity ~6–7 km s^{-1} in CTTS for He I λ6680 line.

---

[5] Line strengths in BEK01 were measured in terms of veiling-corrected equivalent widths since the spectra were not flux-calibrated.

[6] NC and BC kinematics of the CTTS sample are taken from Table 1 of BEK01. The respective mass estimates are not from a uniform source.

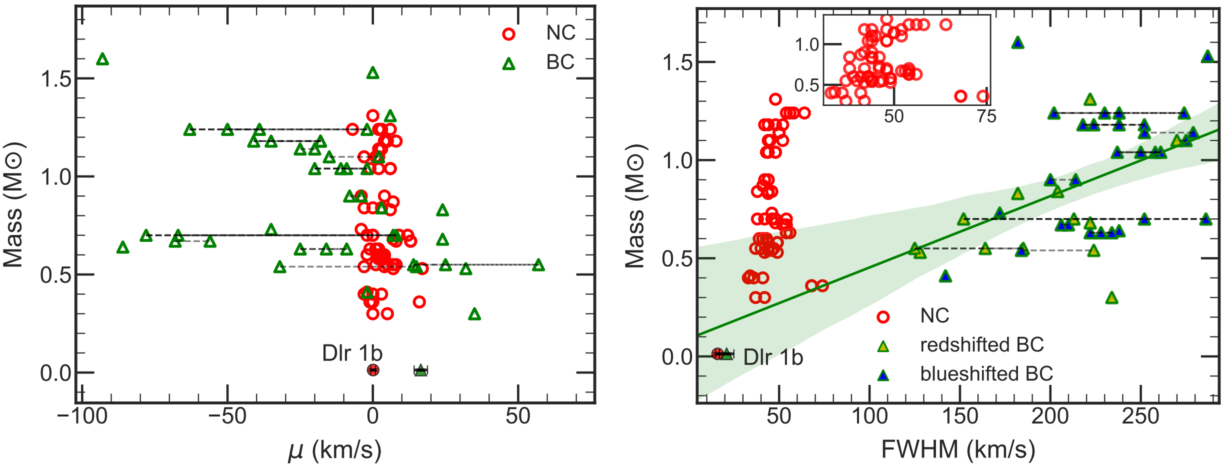

Fig. 3. Distribution of (left) the centroid velocities, μ, and (right) FWHM of He I λ5877 NC (open circles) and BC (open triangles) of the BEK01 sample with respect to their mass estimates, with BC colour-coded with respect to centroid velocities in the right panel. The NC and BC measurements of Delorme 1 (AB)b from this work are shown as filled red and green data points in the figure. The inset in the bottom panel zooms in along the FWHM-axis of NC distribution of the CTTS sample. The linear fit to the BC distribution is shown as a green line, along with its 1σ confidence interval (shaded green region). Measurements from different observations of the same source are joined by dashed black lines in both plots.

4.2. Triplet–singlet line ratios

The triplet line He I λ5877 and the singlet line He I λ6680 share a common upper energy level and are a popular pair in the literature for deciphering the physical conditions of the line emitting region (Schneeberger et al. 1978; BEK01; Gahm et al. 2013). In particular, the ratio of their line intensities can hint at the temperature and density in these regions and whether they are in local thermodynamic equilibrium (LTE; Sicilia-Aguilar et al. 2012). Under nebular conditions, assuming very low electron densities and He I line origin purely from recombination and cascade, the λ5877 emission is expected to be stronger than λ6680 and their line ratio is predicted to be ~3.5 (Brocklehurst 1972; Smits 1996). When collisional excitation contributes at higher densities, this ratio will initially increase but will eventually fall to unity, when thermal equilibrium is reached at very high densities due to coupling between the triplet and singlet levels (BEK01). For Delorme 1 (AB)b, the average of the line ratios λ5877/λ6680 for the respective NCs from individual epochs yields a value of 1.7±0.4, which is close to unity, indicating very high densities and conditions of near thermal equilibrium in the NC-emitting region. This value is very similar to the reported NC line ratio of 2.0±0.6 in BEK01 measured from their CTTS sample. Kwan & Fischer (2011) argue, based on calculations from line excitation models, that the production of optically thick He I λ5877 line emission requires high densities $> 10^{11}$ cm^{-3} and high temperatures $>$ 15 000 K; such physical conditions could be met in the shock generated at the base of accretion columns on the planet surface. BEK01 also finds that the corresponding BC in CTTS has a line ratio similar to the nebular value, indicating formation in lower density conditions, but we refrain from a direct comparison in our work due to the tentative nature of the singlet BC.

The main caveat with inferences drawn from such analysis with line ratios is that the triplet 5877 Å emission line is composed of multiple transitions originating from closely spaced energy levels that occur at very similar wavelengths. The bulk of the observed line emission is dominated by transitions from a slightly lower energy level than the 6680 Å transition, since the corresponding transition from the exact same upper energy level has a much lower transition probability. Thus, more accurate estimates of the physical conditions within the emitting region would require dedicated radiative transfer modelling.

4.3. Accretion luminosity and mass accretion rate

Ringqvist et al. (2023) estimated accretion luminosity (L_{acc}) for Delorme 1 (AB)b from line luminosities (L_{line}) of its Balmer emission, using L_{line}–L_{acc} scaling relations developed based on 1D planet-surface shock models (Aoyama et al. 2021). Similar relations have not been developed for He I emission lines; alternatively, we used the empirical scaling relations for He I lines developed by Fiorellino et al. (2025), updated from those in Alcalá et al. (2017) based on a sample of Class II young stellar objects (YSOs) down to 0.02 $M_{\odot}$, of the form

$$\log L_{\mathrm{acc}} = a \times \log L_{\mathrm{line}} + b, \tag{1}$$

where L_{acc}, L_{line} are in units of $L_{\odot}$. The mean L_{acc} of the He I lines (see Table 3 for individual values) is $\log(L_{\mathrm{acc}}/L_{\odot}) = -4.9 \pm 0.3$.

In ENTROPY II, we showed that the wings component of the Balmer emission lines from the target could originate from gas in accretion columns along magnetic field lines. The NC in the target's He I emission seems to imply physical conditions expected at the accretion shock at the base of these funnels (see Section 4.2). Assuming a magnetospheric accretion geometry from these hints, we derived the corresponding mass accretion rates for the target from the integrated flux of each He I line using the conventional formula for accreting YSOs (Hartmann et al. 2016),

$$\dot{M}_{\mathrm{acc}} = \left(1 - \frac{R}{R_{\mathrm{in}}}\right)^{-1} \frac{L_{\mathrm{acc}} R}{GM}, \tag{2}$$

where R, M represents the radius and mass of the accreting body, which are 0.16 ± 0.01 $R_{\odot}$ and 13±5 M_{Jup} respectively for Delorme 1 (AB)b (Ringqvist et al. 2023). R_{in}, the inner truncation radius, is not well-established for PMOs but is typically set to a standard value of 5R for CTTS (see Bouvier et al. 2007; Hartmann et al. 2016). With $R_{\mathrm{in}} = 5R$, the mean

Table 3. Accretion luminosity of detected He I lines and corresponding mass accretion rates.

$\lambda_{\text{rest, vac}}$ (Å)	$\log(L_{\text{line}}/L_{\odot})$ (dex)	$\log(L_{\text{acc}}/L_{\odot})$ (dex)	$\log(\dot{M}_{\text{acc}}/M_{\text{Jup}}\ \text{yr}^{-1})$ (dex)
4027.33	−8.2 ± 0.2	−5.3 ± 1.0	−8.5 ± 1.0
4472.73	−7.8 ± 0.1	−4.9 ± 0.6	−8.2 ± 0.7
4923.31	−8.3 ± 0.1	−4.8 ± 0.6	−8.1 ± 0.7
5017.08	−8.3 ± 0.1	−4.2 ± 0.7	−7.5 ± 0.7
5877.25	−7.3 ± 0.1	−4.7 ± 0.6	−7.9 ± 0.6
6679.99	−7.7 ± 0.1	−5.3 ± 0.8	−8.5 ± 0.03

Notes. We assume no extinction ($A_v = 0$) for these calculations.

$\dot{M}_{\text{acc}}$ obtained from the He I lines for Delorme 1 (AB)b is $\log(\dot{M}_{\text{acc}}/M_{\text{Jup}}\ \text{yr}^{-1}) = -8.1 \pm 0.3$ (see Table 3 for individual values), i.e. ~$7 \times 10^{-12} M_{\odot}\ \text{yr}^{-1}$. This is comparable to, but slightly higher than the accretion rate derived from its UV excess ($1\text{–}3 \times 10^{-12} M_{\odot}\ \text{yr}^{-1}$; ENTROPY II) using the hydrogen slab model, as well as the $\dot{M}_{\text{acc}}$ derived from the Hα line flux in the spectra using Fiorellino et al. (2025) scaling relations ($1.4 \times 10^{-12} M_{\odot}\ \text{yr}^{-1}$). However, recent studies show that the inner disk radius can be as small as 2–3R for T Tauri stars (see Pittman et al. 2025). Additionally, ENTROPY II shows that magnetospheric accretion models (Thanathibodee et al. 2019) that best fit the Balmer line profiles of Delorme 1 (AB)b predict a smaller R_{in} of 1.5–3R for this PMO. If we assume $R_{\text{in}} = 1.5R$, the mass accretion rate obtained increases to $1.8 \times 10^{-11} M_{\odot}\ \text{yr}^{-1}$, more than twice the value obtained with $R_{\text{in}} = 5R$.

We note that the accretion luminosity and mass accretion rate derived from Hα line flux using planetary scaling relations from Aoyama et al. (2021) are considerably higher than the corresponding estimates from both the UV excess using the slab model (by ~1 dex) and the He I lines using empirical stellar scaling relations from Fiorellino et al. (2025) (by ~0.6 dex). The latter difference could be partially contributed by the extrapolation of the L_{line}–L_{acc} scaling relation for the He I lines to lower mass regimes. However, the significant difference in these estimates indicates that the Aoyama et al. (2018, 2021) shock models may be overestimating the accretion luminosities for wide-orbit planetary companions like Delorme 1 (AB)b, and consequently highlights potential limitations in applying the corresponding scaling relations to protoplanets.

4.4. Correlation with UV excess and Balmer emission

Accretion hotspots, where magnetospheric funnels hit the surface of the accreting source, can give rise to excess emission in the ultraviolet and optical domain. This excess flux can add to the continuum at these wavelengths, giving rise to the veiling effect seen in T Tauri stars. Hence, both UV excess and continuum veiling observed in young stars have been used as strong proxies for ongoing accretion.

The total Hα emission from the target seems to be well correlated with the UV excess (see Fig. 4), with the correlation driven mostly by the wings component (see ENTROPY II). In general, the He I lines detected from the target also display a good correlation with the UV excess similar to Hα. In Fig. 4, we show the correlation plots for the strongest helium line He I D3 with UV excess and Hα. Its correlation is quite strong with the mean UV excess in each epoch (Pearson's $r = 0.90$), and it is even stronger for the NC flux (Pearson's $r = 0.94$), indicating accretion origin. From Fig. 4, we see that the NC and BC flux seem uncorrelated with each other, and consequently, there is a relatively weaker correlation between BC flux and UV excess. However, this is mostly driven by a single epoch – 13 October 2022 – with strong BC flux and low UV excess. Excluding this epoch, the correlation of BC is strong with both UV excess (Pearson's $r = 0.94$, $p = 5 \times 10^{-4}$) and NC flux (Pearson's $r = 0.85$, $p = 0.02$).

He I emission lines from the target also seem to closely follow the variation in the Hα flux through the epochs; for He I D3 this is illustrated in the figure. Among its two components, BC seems to be strongly correlated with Hα, while the correlation is slightly weaker for NC. This behaviour is in contrast to what we see with the UV excess. However, this is yet again driven by the epoch on 13 October 2022, excluding which the correlation becomes much stronger between NC and Hα (Pearson's $r = 0.94$, $p = 5 \times 10^{-5}$). We note here that we also attempted the empirical, non-Gaussian decomposition developed for the target's Balmer profiles in ENTROPY II, on the helium lines in this work, to compare the respective wings and core components of He I D3 and Hα. However, the wings component appears only in a few epochs for He I D3 in the resulting profile fits. Moreover, the velocity scales are vastly different for the two lines, as well as the resulting wings components; the entire He I D3 profile spans from −25 to +60 km s^{-1}, which is only slightly wider than the FWHM (~70 km s^{-1}) of the Class A Hα profile. Hence, we adhere to the usual Gaussian decomposition and refrain from any comparison with the individual wings and/or core components of Hα.

Fig. 5 provides a comparison of accretion luminosity derived from He I and Hα line flux using Fiorellino et al. (2025) scaling relations with the value derived in ENTROPY II from UV excess emission using hydrogen slab models; the latter is a robust estimation of an upper limit on accretion luminosity as it is independent of the inherent uncertainties of the empirical L_{line}–L_{acc} scaling relations. The figure demonstrates that the value of L_{acc} derived from the integrated Hα flux is relatively consistent with the value derived from the UV excess, although slightly lower. Among the He I lines, the L_{acc} derived from the He I λ6680 line flux is highly consistent with the estimate from the UV excess, while those from the asymmetric He I lines $\lambda\lambda$5877, 4923, 4473 are generally slightly higher, with the difference being the highest for He I D3; the difference between $\dot{M}_{\text{acc}}$ obtained from He I λ6680 and He I D3 is a factor of 4 (see Table 3). The slightly higher values for L_{acc} estimates from these He I lines could point to a likely contribution of chromospheric activity. However, the deviation in the L_{acc} values could also be attributed to uncertainties stemming from the empirical L_{line}–L_{acc} scaling relations. These relations are based on accretors of much higher mass than the target; although the sample in Fiorellino et al. (2025) goes down to 0.02 $M_{\odot}$, there is only one low-mass target in the entire sample.

4.5. Comparison to He I emission in the primary

The VLT/UVES observations also provide the spectra of the target's M5-type host binary, Delorme 1 AB, which is non-accreting; it does not show any UV excess in its spectra and has no confirmed disk around it. Emission lines in the primary's spectra, attributed solely to chromospheric activity, and taken with the same instrument at the same epochs, serve as a good tool to gauge the contribution to the companion's spectra from activity. We detected both the popular activity indicators Hα and He I D3 in emission from the primary spectra, the latter

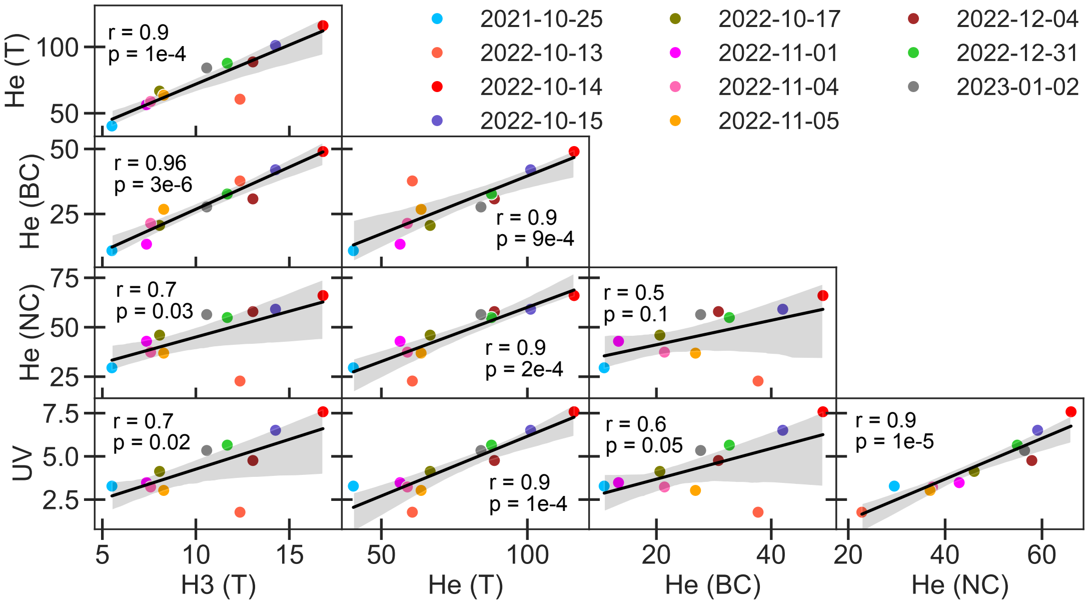

Fig. 4. Correlations between He I $\lambda5877$ line flux measured in this work, and Hα line flux and UV excess reported in ENTROPY II. The He I and UV flux are in units of 10^{-17} cgs and Hα are in units of 10^{-15} cgs. The Pearson's correlation coefficients (r) and the corresponding p-values are given in each plot. For both He I and Hα, 'T' denotes the total flux integrated over their entire profile.

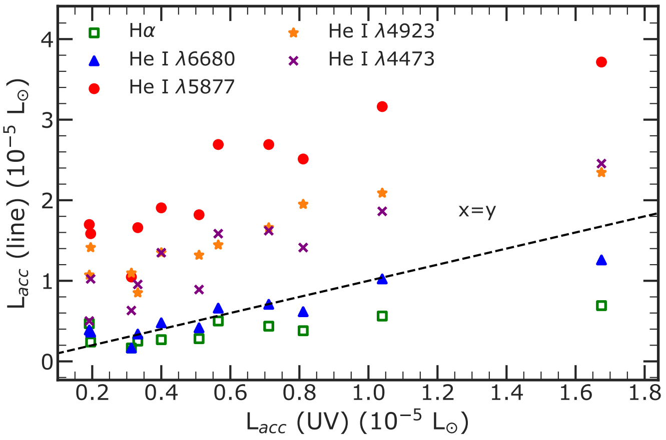

Fig. 5. Accretion luminosity measurements of Delorme 1 (AB)b derived from He I and Hα lines from each of the 11 nights using $L_{\rm line}$–$L_{\rm acc}$ scaling relations from Fiorellino et al. (2025), plotted against the respective values measured from UV excess reported in ENTROPY II.

at ~4σ. The centroid velocity of He I D3 is small and redshifted (2.2 ± 0.2 km s^{-1}), but its line profile is symmetric about the centre, unlike the line profile of the companion. He I emission at $\lambda\lambda4027, 4473$ was also detected from the primary at 5σ and 7σ respectively, similar to previous detections from M-type dwarfs (e.g. Di Maio et al. 2020), but no asymmetry was detected in either of the line profiles. Unlike the Balmer and He I emission lines from the PMC, which show strong flux variation between the individual epochs as expected from accretion, Hα and He I lines from its primary show relatively uniform flux levels between the epochs, with the exception on 2 January 2023 where all lines show an overall increase in flux by a factor 1.5 to 2, accompanied by enhanced flux in the blue wing (see Fig. E.1). Such blue wing asymmetries are typical during flares from similar M-dwarfs (Notsu et al. 2024). This epoch also shows the tentative appearance of He I emission lines $\lambda\lambda3820, 4923, 6680$ from the primary. He I $\lambda6680$ emission is usually observed from CTTS and is associated with accretion (Muzerolle et al. 1998), but it has been reported from M-type main sequence stars during flare maximum, along with He I emission at $\lambda4923$ (Bleach et al. 2002). The mean $L_{\rm acc}$ measured from the He I lines in the primary spectra is $\log(L_{\rm acc}/L_\odot) = -4.2 \pm 0.1$ and the corresponding accretion rate $\log(\dot{M}_{\rm acc}/M_\odot\ {\rm yr}^{-1}) = -11.4 \pm 0.1$ (assuming $R_{\rm in} = 5R$). Overall, the nature of the primary's He I line profiles from activity presents a stark contrast to those observed from the companion, further hinting at accretion origin for the latter.

5. Discussion

5.1. Origin of NC and BC

Asymmetries in the He I line profiles are commonly found in the accretion signatures of CTTS. While the NC is interpreted as tracing the accretion shock at the stellar surface in these objects, the exact origin of BC remains inconclusive in the literature, with attributions to both hot-wind origin (for blueshifted BC) and accretion-flow origin (see Edwards 2003; Armeni et al. 2024). In Section 4, we used a few diagnostic tools to obtain clues about the possible physical origins of the narrow and broad components detected from the He I line profiles of the target, which we discuss below.

A comparison of the profile characteristics of the target's He I D3 emission line to those of CTTS (see Section 4.1) reveals that, while the NC width is much narrower than the typical width seen in CTTS, the slightly redshifted mean NC centroid velocity (0.1 ± 0.8 km s^{-1}) is well within the expected range among CTTS, and could point to emission from a post-shock region. The epoch-to-epoch variation of the NC centroid velocity (see Fig. 2), oscillating mostly between ±1 km s^{-1}, is also strongly indicative of its formation close to the planet's surface. Such velocity oscillations observed in T Tauri stars are consistent with the NC tracing a hot spot localised at high latitudes on the stellar surface and corresponding to the accretion shock at the bottom of an accretion column in a dipolar geometry (McGinnis et al. 2020). The triplet–singlet line ratio derived in Section 4.2 for the He I D3 NC also implies high densities and near-thermodynamic equilibrium conditions within the line formation regions, which are typical of such post-shock regions.

The strong correlation of He I D3 NC with the UV excess emission from the target also corroborates an accretion-related origin for the NC emission in general; however, UV excess emission can have contributions from chromospheric activity in stars, which may result in a similar correlation. The near-UV flux from Delorme 1 (AB)b ($F_\lambda = 2$–10×10^{-17} erg s^{-1} cm^{-2} Å^{-1} at 3500 Å; see ENTROPY II) is in the range of the expected level of chromospheric activity among late M-dwarfs ($M_\star > 0.08\ M_\odot$) older than 10 Myr, as reported in Richey-Yowell et al. (2023). Their analysis, however, does not distinguish accretors from non-accretors beyond 10 Myr, whereas accretion has been seen to proceed quite late into the formation stage among lower-mass objects like Delorme 1 (AB)b. Additionally, BEK01 showed that the He I D3 NC flux from their CTTS sample, attributed to post-shock origin, is strongly correlated with the continuum veiling produced by UV excess. Furthermore, Kwan (2024) showed that for the He I D3 profiles among the BEK01 sample with stronger NC, accretion shock models can reproduce both their NC flux and the UV continuum excess.

The BC in the He I D3 emission from the target seems to be of a much lower width compared to those in CTTS, but this may be explained by the much lower mass of the target compared to CTTS. Although the BC is mostly blueshifted among CTTS, its centroid velocity in the target spectra is within the range of the few redshifted BCs in these sources. The detection of similar BCs in the singlet transition He I λ4923, as well as the variation in the BC/NC flux ratio through the epochs, implies that this asymmetry is not simply from the resolution of the triplet components in the emission line. This is slightly corroborated by the lack of asymmetry in the primary's He I D3 emission, although there is a possibility in the case of the primary that the line may simply be intrinsically wider than the velocity separation between its triplet components to produce this asymmetry. However, redshifted BCs have been found in CTTS despite large line widths. The strong correlation with UV excess on excluding the 13 October 2022 epoch is also suggestive of an origin from accretion-related processes.

We saw in Section 3.4 that the centroid velocity of the BC shares a strong correlation in time with that of the NC. This hints at a common mechanism of origin for these two components, likely within the post-shock region. This is further corroborated by the fact that we see the BC persistently redshifted in our multi-epoch observations, oscillating closely around ~+15 km s^{-1}. Such behaviour is expected from accretion-shock emission from near the planet surface; if the rotational velocity is less than the velocity of the infalling gas, then we may not catch a blueshift but simply observe the BC oscillate around a redshift. The FWHM of the BC tells us that the bulk of its emission is coming from the gas that is moving at ~20–30 km s^{-1}, which implies an origin close to the surface of the planet. Instead, if the BC originates within the accretion-flow as proposed for CTTS, its width should be compatible with the free-fall or Keplerian velocity of the gas. For Delorme 1 (AB)b, the free-fall velocity at its surface is 176 km s^{-1} and the infall velocity of gas falling from a distance of $R_{\rm in} = 2R$ is 124 km s^{-1}. Assuming a distance range from $R_{\rm in} = 3R$ to the planet surface, the Keplerian velocity will range from 72–124 km s^{-1}, with its projection along the line of sight (assuming a typical inclination of 60°) 62–108 km s^{-1}. The He I BC width for the target is much narrower than these estimates, rendering emission from the accretion flow unlikely.

Alternatively, the asymmetry in the red wing seen in the target's He I profiles could be a part of the NC line profile. Pure-NC profiles among CTTS have been seen to display some asymmetry in the red part of the line profile due to velocity gradients in the post-shock region, resulting from the incoming gas experiencing a strong deceleration as it approaches the surface of the accretor (see Donati et al. 2008, 2012, 2013). In fact, some of the pure-NC profiles in BEK01 show a similar asymmetry, and the extracted NCs from composite profiles in their sample show on average a redwing asymmetry very similar to what is seen from Delorme 1 (AB)b. This is further supported by the slightly asymmetric NC profile of He I λ6680 from Delorme 1 (AB)b. Such an origin may explain the strong correlation seen between NC and BC parameters of these He I lines from the target. However, asymmetry resulting from such velocity gradients in the He I D3 line usually exhibits a smooth profile with an extended red wing and a steep blue wing (see Nowacki et al. 2023; Armeni et al. 2024). Although this may be descriptive of the profile asymmetries in the higher He I transitions $\lambda\lambda$4923, 4473, 4027 from the target, the asymmetry in the observed He I D3 line manifests itself as a clear 'bump' in the red wing, which is more suggestive of an additional component in the profile.

Thus, it is very likely that BC is also formed within the temperature-stratified shock structure, but closer to the shock front than the NC, where the temperature is higher and the gas is still infalling. NC could be formed at a lower temperature region within the shock structure, closer to the planet surface.

5.2. Accretion or activity?

Evidence of ongoing accretion at Delorme 1 (AB)b at its age of ~40 Myr emphasizes the challenges in understanding the formation of wide-orbit planetary-mass companions. Mâlin et al. (2025) studied the mid-infrared spectra of the target and showed that its CPD retains a significant amount of gas, despite being older than the typical time scales for gas dispersion around low-mass stars. Stamatellos & Herczeg (2015) found that low-mass bound companions, which form via fragmentation of their parent circumstellar disk, can assemble more massive disks around them than previously expected, which evolve slower in time at low viscosities. Betti et al. (2023) further deduced that the mass accretion rates for PMCs do not fall as steeply with decreasing mass as in the case of stars and brown dwarfs. An important step in understanding these new trends emerging at planetary masses is to exercise caution and accuracy in determining accretion characteristics, especially distinguishing accretion signatures from those of activity.

Both Hα and He I D3 are popular indicators of chromospheric activity among late-type stars and YSOs (Saar et al. 1997; Rachford 1997). In CTTS, such emission from activity can augment the line emission originating in the infalling gas from an accretion disk (Petrov et al. 2011; Manara et al. 2013). It is crucial to gauge this contribution while determining the accretion properties in lower mass regimes, where the accretion levels are weak ($L_{\rm acc} < 10^{-3} L_\odot$).

In Fig. 6, we compare the emission level measured from the target to those of known accreting objects from Betti et al. (2023, CASPAR), as well as non-accreting Class III YSOs and field M-dwarfs with activity-induced line emission. The upper panel

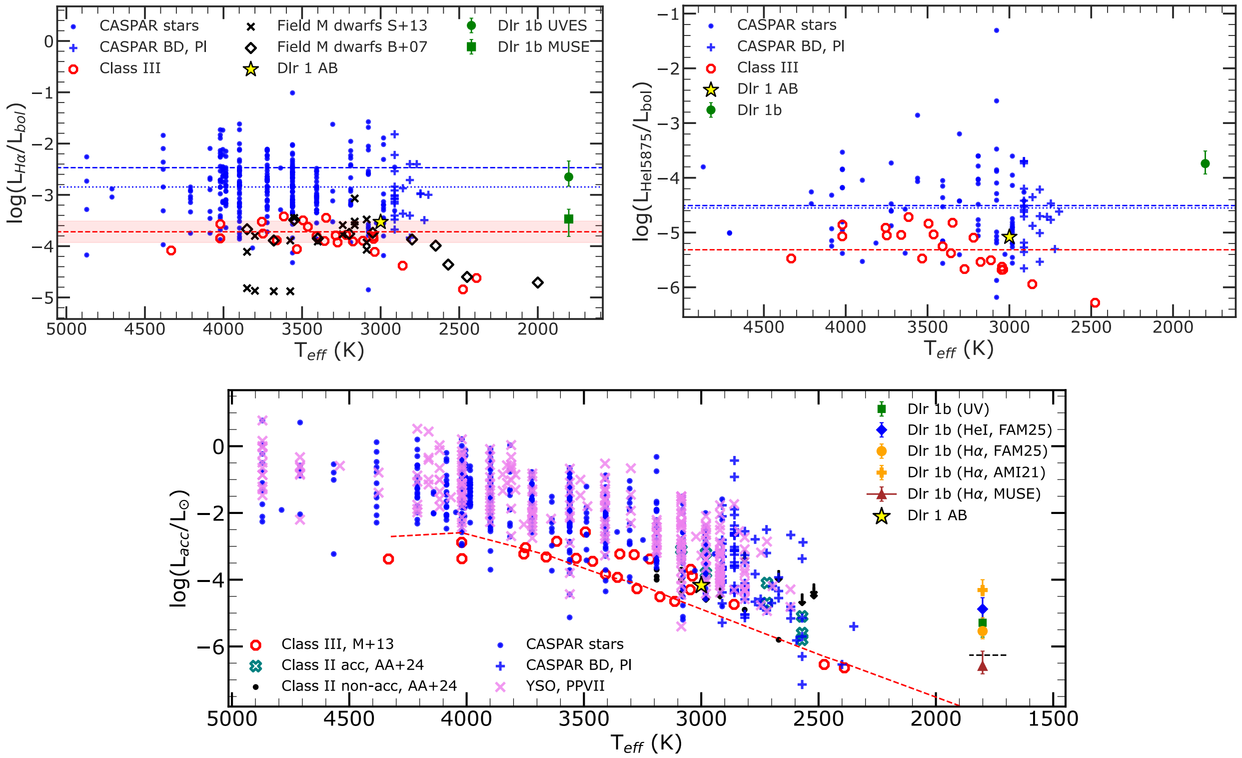

Fig. 6. Top: fractional Hα (left) and He I λ5877 (right) luminosity of Delorme 1 (AB)b (filled green circle) shown with respective values from the CASPAR sample of young stars, brown dwarfs, and planets ('BD', 'Pl'), sample of active field M-dwarfs from Stelzer et al. (2013b) and Bochanski et al. (2007), and sample of Class III non-accretors from Manara et al. (2013). The available Hα measurement for the target with MUSE is shown as the filled green square. The dashed red line (shaded region denotes error bars) shows the mean activity index for Hα (Stelzer et al. 2013a) and He I (this work). The blue lines denote the median measurements for CASPAR stars (dotted) and brown dwarfs, planets (dashed). Bottom: accretion luminosity of Delorme 1 (AB)b measured from UV excess, He I lines, and Hα, along with Class III sources from Manara et al. (2013) and CASPAR accretors. Also shown are low-mass Class II accretors (unfilled teal crosses) and non-accretors (black dots, with upper limits as downward arrows) from Almendros-Abad et al. (2024) and a sample of accreting YSOs from seven star-forming regions from Manara et al. (2023) (pink crosses). $T_{\rm eff}$–$L_{\rm acc,noise}$ relation from Manara et al. (2013) is shown as the dashed red curve, and the $L_{\rm acc,noise}$ from Venuti et al. (2019) at 20 $M_{\rm Jup}$ is shown as the dashed black line. FAM25 and AMI21 denotes $L_{\rm line}$–$L_{\rm acc}$ scaling relations from Fiorellino et al. (2025) and Aoyama et al. (2021) respectively, and $L_{\rm acc}$ derived from MUSE epoch is denoted as the brown triangle. In all the panels, measurements from the primary are denoted as a yellow star and fall very close to the measurements from non-accretors.

illustrates the sharply decreasing activity level at late spectral types for the Class III sample, for both Hα and He I D3 line emission. The fractional Hα luminosity measured from Delorme 1b with UVES, $\log(L_{\rm H\alpha}/L_{\rm bol}) = -2.65^{+0.31}_{-0.18}$[7], is more than 1 dex above the mean activity index of the Class III sample (-3.72 ± 0.21; Stelzer et al. 2013a), and agrees well with the median measurements of CASPAR accretors. The median He I fractional luminosity measured in this work, $\log(L_{\rm He\,I}/L_{\rm bol}) = -3.74^{+0.23}_{-0.19}$, is also well above the median Class III measurement (−5.31), and slightly higher than those of CASPAR accretors (∼−4.5). This indicates that the Hα and He I line emission in these UVES observations is clearly dominated by accretion. However, the target's MUSE observations in September 2018 report a much lower Hα flux with $\log(L_{\rm H\alpha}/L_{\rm bol}) = -3.47^{+0.19}_{-0.34}$, putting it right near the mean activity index. This suggests that Delorme 1 (AB)b, being a weak accretor ($\dot{M}_{\rm acc} \sim 10^{-12} M_\odot {\rm yr}^{-1}$), might have been activity-dominated in the MUSE epoch; in other words, accretion at the target might be highly episodic. Notably, the MUSE epoch lacks He I line detections, except for very weak detections of λ6680 and λ7065.

For such weak accretors, Manara et al. (2013) empirically defines the minimum accretion luminosity that can be measured from line emission, $L_{\rm acc,noise}$, below which the line emission is likely to be dominated by chromospheric activity. This relation for 'chromospheric noise', based on a sample of Class III YSOs up to spectral type M9.5, is given as

$$\log(L_{\rm acc,noise}/L_\star) = (6.17 \pm 0.53) \log T_{\rm eff} - (24.54 \pm 1.88), \quad (3)$$

where $L_\star$ is the bolometric luminosity of the object and $T_{\rm eff}$ is its effective temperature in kelvin. In line with expectations, the mean $L_{\rm acc}$ measured from the non-accreting central binary is within ∼0.6 dex of the predicted $L_{\rm acc,noise}$ (−4.74) at its temperature (3000 K; Ringqvist et al. 2023). By extrapolating this relation to the target's temperature of 1801 K (with $\log(L_\star/L_\odot) = -3.58$; Eriksson et al. 2020), we get $\log(L_{\rm acc,noise}/L_\odot) = -8.03$. The $L_{\rm acc}$ derived for the target from the Hα and He I lines (see Table F.1 for the values) are, respectively, 2.5 dex and 3.2 dex higher than this limit. This is illustrated in the bottom panel of Fig. 6. We note that the $L_{\rm acc}$ measured from the target's Hα flux from MUSE observations also falls well above the $L_{\rm acc,noise}$. As an added measure of extrapolation, we also compared the $L_{\rm acc}$ from the He I lines to the $L_{\rm acc,noise}$ of the two least massive objects (∼20 $M_{\rm Jup}$) in the Class III sample – M9-type TWA 26 and M9.5-type TWA 29. Both of these objects have

---

[7] The error bars on the fractional luminosity and accretion luminosity measurements correspond to the lowest and highest values during the observation epochs.

$\log(L_{\rm acc,noise}/L_\odot) \sim -6.6$, which is still 1.7 dex below the target's $L_{\rm acc}$, adding confidence to the inference from the extrapolated relation above.

Independently, Venuti et al. (2019) estimated the mass-dependent noise threshold, $\dot{M}_{\rm acc,noise}$, for YSOs down to 20 $M_{\rm Jup}$ at 10 Myr based on $L_{\rm acc}$ measurements of 11 non-accreting stars in the TWA stellar association. At 20 $M_{\rm Jup}$, they predict $\dot{M}_{\rm acc,noise} \sim 3 \times 10^{-13} M_\odot\ {\rm yr}^{-1}$, which is ~1 dex lower than the estimated mass accretion rates for Delorme 1 (AB)b with UVES. In Fig. 6 (bottom panel), we show the corresponding $L_{\rm acc,noise}$; at the MUSE epoch the target clearly falls below this threshold, underlining the earlier inference that the 2018 observations could have been activity-dominated.

Additionally, for accretion luminosities measured from UV continuum excess, Claes et al. (2024) developed a parallel relation for $L_{\rm acc,noise}$, given by

$$\log(L_{\rm acc,noise}/L_\star) = (5.9 \pm 0.2) \log(T_{\rm eff}[{\rm K}]) - (23.3 \pm 0.7). \quad (4)$$

If $L_{\rm acc}$ falls below this threshold, the observed UV excess alone cannot determine that the target is accreting. At the target's temperature, this threshold value is −7.67, which is more than 2 dex below the measured $L_{\rm acc}$ from the target's UV continuum excess (see Table F.1). Thus, the UV continuum excess and the Hα and He I line emission detected in these UVES observations are clearly dominated by accretion processes. However, as discussed in Section 4.4, the contribution to the He I lines from chromospheric activity cannot be dismissed, although not prominent.

6. Conclusions

In this study, we continued our analysis of the high-resolution optical to near-UV spectra of Delorme 1 (AB)b from ENTROPY II, focusing on helium emission from this planetary-mass object. We presented resolved line profiles of seven He I emission lines detected with high confidence from the target, including the prominent accretion tracers in CTTS, He I $\lambda\lambda$5877, 6680. All detected He I lines show moderate flux variation over time, similar to He I profiles in CTTS. The median line profiles of He I $\lambda\lambda$5877, 4923, 4473, and 4027 display clear asymmetry with a narrow and broad component; the latter is redshifted, unlike commonly observed in CTTS. Analysis of NC behaviour in He I D3 is strongly suggestive of formation within the immediate post-shock region close to the surface of the planet. The BC is most likely of an accretion origin, and its strong correlation in velocity with the NC and the line widths suggest an origin within the shock structure, but closer to the shock front, at higher temperatures. It could also be an asymmetry in the red part of a pure-NC line profile due to a velocity gradient in the post-shock region. Comparison of fractional luminosity $L_{\rm He\ I}/L_{\rm bol}$ and $L_{\rm acc}$ from He I flux with those of higher-mass non-accretors indicates that He I emission is accretion-dominated in these observations, but contribution from activity cannot be completely dismissed.

A key factor in analysing the accretion signatures of such low-mass objects is to gauge the level of contribution from chromospheric activity at these low $T_{\rm eff}$ values or masses. Currently, records of activity indicators from field dwarfs and Class III sources extend up to late M-types, with few sources cooler than $T_{\rm eff}$ = 2500 K, as demonstrated in this work. Although the general trend from higher mass non-accretors indicates a steep decline in activity level at late spectral types, the level of activity at low $T_{\rm eff}$ ranges as Delorme 1 (AB)b remains unclear; the extrapolation of the Manara et al. (2013) relation to much lower $T_{\rm eff}$ such as for the target is not really justified since the atmosphere becomes mostly neutral at these temperatures, making activity diagnostics unreliable (Mohanty & Basri 2003). Observations of more low-mass Class III sources are as equally vital as observations of emission signatures from accretors to understand accretion in the planetary-mass regime. The target sample of the approved VLT/UVES program ENTROPY (PI: Bonnefoy) is designed to tackle exactly this need and will search for prominent accretion indicators, including optical helium line emission, from both accreting and non-accreting sources below 20 $M_{\rm Jup}$.

The He I λ10 833 emission line is another significant accretion tracer among CTTS in the near-infrared that is sensitive to both accretion and accretion-related outflows such as disk wind or stellar wind (Edwards et al. 2006; Kwan et al. 2007; Erkal et al. 2022). It has recently been detected in a very low-mass object, TWA 27b (see Luhman et al. 2023; Marleau et al. 2024), using the JWST Near-Infrared Spectrograph (NIRSpec; Jakobsen et al. 2022). The CRyogenic high-resolution InfraRed Echelle Spectrograph (CRIRES; Kaeufl et al. 2004) at VLT can observe the He I λ10 833 line at a high spectral resolution of $R_\lambda \geq 50\,000$ required to disentangle accretion features in the line profile. The upcoming ArmazoNes high Dispersion Echelle Spectrograph (ANDES; Marconi et al. 2024) at the Extremely Large Telescope (ELT) that will see its first light early in the next decade has the potential to observe helium emission from protoplanets from near-UV to near-infrared, covering several of the prominent accretion tracers. Such observations will pave the way for population-level studies to understand helium emission from PMOs and can support the development of accretion models, as has been done for hydrogen emission, sculpting the accretion geometry of protoplanets.

Data availability

The underlying data used for this work are the flux-calibrated 1D UVES spectra obtained from the ESO observations from 13 October 2022 to 2 January 2023 (programme 0110.C-0203(A)) and on 25 October 2021 (programme 0108.C-0655(A)). Raw science data and calibration products are available through ESO Archive Services. The median stacked He I line profiles are available through Zenodo `10.5281/zenodo.19006669`.

Acknowledgements. We acknowledge support in France from the French National Research Agency (ANR) through project grant ANR-20-CE31-0012. We thank Justyn Campbell-White for his valuable inputs and discussions on this work. G.V. acknowledges support from the Swedish Research Council (*SRC*) via the International Postdoc Grant for the project GENESIS (2024-06609). G.-D.M. acknowledges the support of the Deutsche Forschungsgemeinschaft (DFG) through grant MA 9185/2-1.

References

Alcalá, J. M., Manara, C. F., Natta, A., et al. 2017, A&A, 600, A20
Almendros-Abad, V., Manara, C. F., Testi, L., et al. 2024, A&A, 685, A118
Almendros-Abad, V., Scholz, A., Damian, B., et al. 2025, ApJ, 992, L2
Aoyama, Y., Ikoma, M., & Tanigawa, T. 2018, ApJ, 866, 84
Aoyama, Y., Marleau, G.-D., Ikoma, M., & Mordasini, C. 2021, ApJ, 917, L30
Aoyama, Y., Marleau, G.-D., & Hashimoto, J. 2024, AJ, 168, 155
Armeni, A., Stelzer, B., Frasca, A., et al. 2024, A&A, 690, A225
Arulanantham, N., Gronke, M., Fiorellino, E., et al. 2023, ApJ, 944, 185
Bacon, R., Accardo, M., Adjali, L., et al. 2010, SPIE Conf. Ser., 7735, 773508
Ballester, P., Modigliani, A., Boitquin, O., et al. 2000, The Messenger, 101, 31
Beristain, G., Edwards, S., & Kwan, J. 2001, ApJ, 551, 1037
Betti, S. K., Follette, K. B., Ward-Duong, K., et al. 2022, ApJ, 935, L18
Betti, S. K., Follette, K. B., Ward-Duong, K., et al. 2023, AJ, 166, 262

Bleach, J. N., Wood, J. H., Smalley, B., & Catalán, M. S. 2002, MNRAS, 335, 593
Bochanski, J. J., West, A. A., Hawley, S. L., & Covey, K. R. 2007, AJ, 133, 531
Boucher, A., Lafrenière, D., Gagné, J., et al. 2016, ApJ, 832, 50
Bouvier, J., Alencar, S. H. P., Harries, T. J., Johns-Krull, C. M., & Romanova, M. M. 2007, in Protostars and Planets V, eds. Reipurth, B., Jewitt, D., & Keil, K., 479
Brocklehurst, M. 1972, MNRAS, 157, 211
Campbell-White, J., Sicilia-Aguilar, A., Manara, C. F., et al. 2021, MNRAS, 507, 3331
Campbell-White, J., Manara, C. F., Benisty, M., et al. 2023a, ApJ, 956, 25
Campbell-White, J., Manara, C. F., Sicilia-Aguilar, A., et al. 2023b, A&A, 673, A80
Chinchilla, P., Béjar, V. J. S., Lodieu, N., Zapatero Osorio, M. R., & Gauza, B. 2021, A&A, 645, A17
Claes, R. A. B., Campbell-White, J., Manara, C. F., et al. 2024, A&A, 690, A122
Currie, T., Hashimoto, J., Aoyama, Y., et al. 2025, ApJ, 990, L42
Dekker, H., D'Odorico, S., Kaufer, A., Delabre, B., & Kotzlowski, H. 2000, SPIE Conf. Ser., 4008, 534
Del Zanna, G., Storey, P. J., Badnell, N. R., & Andretta, V. 2020, ApJ, 898, 72
Delorme, P., Gagné, J., Girard, J. H., et al. 2013, A&A, 553, L5
Demars, D., Bonnefoy, M., Dougados, C., et al. 2023, A&A, 676, A123
Demars, D., Bonnefoy, M., Dougados, C., et al. 2026, A&A, 706, A57
Di Maio, C., Argiroffi, C., Micela, G., et al. 2020, A&A, 642, A53
Donati, J.-F., Jardine, M. M., Gregory, S. G., et al. 2008, MNRAS, 386, 1234
Donati, J.-F., Gregory, S. G., Alencar, S. H. P., et al. 2012, MNRAS, 425, 2948
Donati, J.-F., Gregory, S. G., Alencar, S. H. P., et al. 2013, MNRAS, 436, 881
Edwards, S. 2003, Astrophys. Space Sci., 287, 47
Edwards, S., Fischer, W., Hillenbrand, L., & Kwan, J. 2006, ApJ, 646, 319
Eriksson, S. C., Asensio Torres, R., Janson, M., et al. 2020, A&A, 638, L6
Erkal, J., Manara, C. F., Schneider, P. C., et al. 2022, A&A, 666, A188
Fiorellino, E., Alcalá, J. M., Manara, C. F., et al. 2025, A&A, 704, A42
Gahm, G. F., Stempels, H. C., Walter, F. M., Petrov, P. P., & Herczeg, G. J. 2013, A&A, 560, A57
Gaia Collaboration (Vallenari, A., et al.) 2023, A&A, 674, A1
Haffert, S. Y., Bohn, A. J., de Boer, J., et al. 2019, Nat. Astron., 3, 749
Hartmann, L., Herczeg, G., & Calvet, N. 2016, ARA&A, 54, 135
Hashimoto, J., & Aoyama, Y. 2025, AJ, 169, 93
Herczeg, G. J., Chen, Y., Donati, J.-F., et al. 2023, ApJ, 956, 102
Högbom, J. A. 1974, A&AS, 15, 417
Jakobsen, P., Ferruit, P., Alves de Oliveira, C., et al. 2022, A&A, 661, A80
Jayawardhana, R., Mohanty, S., & Basri, G. 2003, ApJ, 592, 282
Kaeufl, H.-U., Ballester, P., Biereichel, P., et al. 2004, SPIE Conf. Ser.,. 5492, 1218
Kraus, A. L., Shkolnik, E. L., Allers, K. N., & Liu, M. C. 2014, AJ, 147, 146
Kwan, J. 2024, MNRAS, 531, 3744
Kwan, J., & Fischer, W. 2011, MNRAS, 411, 2383
Kwan, J., Edwards, S., & Fischer, W. 2007, ApJ, 657, 897
Luhman, K. L., Tremblin, P., Birkmann, S. M., et al. 2023, ApJ, 949, L36
Mâlin, M., Ward-Duong, K., Grant, S. L., et al. 2025, A&A, 704, A181
Manara, C. F., Testi, L., Rigliaco, E., et al. 2013, A&A, 551, A107
Manara, C. F., Ansdell, M., Rosotti, G. P., et al. 2023, in Astronomical Society of the Pacific Conference Series, 534, Protostars and Planets VII, eds. Inutsuka, S., Aikawa, Y., Muto, T., Tomida, K., & Tamura, M., 539
Marconi, A., Abreu, M., Adibekyan, V., et al. 2024, SPIE Conf. Ser., 13096, 1309613
Marleau, G.-D., Aoyama, Y., Hashimoto, J., & Zhou, Y. 2024, ApJ, 964, 70
McGinnis, P., Bouvier, J., & Gallet, F. 2020, MNRAS, 497, 2142
Mohanty, S., & Basri, G. 2003, ApJ, 583, 451
Mohanty, S., Jayawardhana, R., & Barrado y Navascués, D. 2003, ApJ, 593, L109
Mohanty, S., Jayawardhana, R., & Basri, G. 2005, ApJ, 626, 498
Muzerolle, J., Hartmann, L., & Calvet, N. 1998, AJ, 116, 455
Muzerolle, J., Luhman, K. L., Briceño, C., Hartmann, L., & Calvet, N. 2005, ApJ, 625, 906
Notsu, Y., Kowalski, A. F., Maehara, H., et al. 2024, ApJ, 961, 189
Nowacki, H., Alecian, E., Perraut, K., et al. 2023, A&A, 678, A86
Petrov, P. P., Gahm, G. F., Stempels, H. C., Walter, F. M., & Artemenko, S. A. 2011, A&A, 535, A6
Pittman, C. V., Espaillat, C. C., Zhu, Z., et al. 2025, ApJ, 993, 181
Rachford, B. L. 1997, ApJ, 486, 994
Richey-Yowell, T., Shkolnik, E. L., Schneider, A. C., et al. 2023, ApJ, 951, 44
Ringqvist, S. C., Viswanath, G., Aoyama, Y., et al. 2023, A&A, 669, L12
Saar, S. H., Huovelin, J., Osten, R. A., & Shcherbakov, A. G. 1997, A&A, 326, 741
Santamaría-Miranda, A., Cáceres, C., Schreiber, M. R., et al. 2018, MNRAS, 475, 2994
Santamaría-Miranda, A., Cáceres, C., Schreiber, M. R., et al. 2019, MNRAS, 488, 5852
Schneeberger, T. J., Linsky, J. L., & Worden, S. P. 1978, A&A, 62, 447
Sicilia-Aguilar, A., Kóspál, Á., Setiawan, J., et al. 2012, A&A, 544, A93
Sicilia-Aguilar, A., Campbell-White, J., Roccatagliata, V., et al. 2023, MNRAS, 526, 4885
Smits, D. P. 1996, MNRAS, 278, 683
Stamatellos, D., & Herczeg, G. J. 2015, MNRAS, 449, 3432
Stelzer, B., Frasca, A., Alcalá, J. M., et al. 2013a, A&A, 558, A141
Stelzer, B., Marino, A., Micela, G., López-Santiago, J., & Liefke, C. 2013b, MNRAS, 431, 2063
Szulágyi, J., & Ercolano, B. 2020, ApJ, 902, 126
Temmink, M., van Dishoeck, E. F., Grant, S. L., et al. 2024, A&A, 686, A117
Thanathibodee, T., Calvet, N., Bae, J., Muzerolle, J., & Hernández, R. F. 2019, ApJ, 885, 94
Ulrich, R. K., & Wood, B. C. 1981, ApJ, 244, 147
Venuti, L., Stelzer, B., Alcalá, J. M., et al. 2019, A&A, 632, A46
Viswanath, G., Ringqvist, S. C., Demars, D., et al. 2024, A&A, 691, A64
Wells, M., Pel, J.-W., Glasse, A., et al. 2015, PASP, 127, 646

Appendix A: Variation in the UVES spectra of Delorme 1 (AB)b

A by-eye classification of the shape and intensity of the Hα emission line reveals three distinct classes of profiles as mentioned in Section 3. Class A profiles displayed during the 2021 epoch as well on 1, 4, and 5 November 2022 are marked by low intensities, with plateau-like cores and no notable deviation in the wings from that of a Gaussian profile. Class A epochs span a total of ~6.2 hr of total integration time over the observations. There is very little flux variability between these individual class A epochs in 2022, with a maximum of ~40% increase on 5 November 2022 compared to 25 October 2021. In comparison, there is notable flux increase on the nights of 13 October, 4 December, and 31 December 2022 and 2 January 2023, with shallow sloping core profiles – we classify these as class B (4.1 hr of total integration time). On 14, 15, and 17 October 2022 (3.3 hr of total integration time), the Hα profile displays a significant increase in the blue wing of the profile compared to both class A and class B profiles. We call these the class C profiles. Top panel of Fig. A.1 illustrates the difference between the three profile classes in terms of their respective median profiles. The bottom panel shows these line profiles normalised with respect to their respective peak intensities, and demonstrate that class A and class B profiles mostly differ in flux levels but share similar profile shapes. Compared to these classes, class C profiles vary largely in flux between individual epochs. The significant rise in Balmer emission during these epochs is also reflected in the respective UV excess and the continuum level beyond ~5300 Å (see Fig. A.2), possibly tracing an accretion burst or chromospheric activity burst. The peak outburst is expected to be around 14 October 2022, showing ~130% increase in Hα intensity compared to 17 October 2022.

Appendix B: Tentative He I detection

From a slightly higher energy level (E_k = 24.21 eV) than the rest of the He I detections in the spectra, He I λ3821 emission is detected tentatively in the grand median at a confidence of 2σ (see Fig. B.1). It is barely present in the class A epochs (0.5σ), but appears in the class B and class C epochs (1.4σ), with maximum intensity in class C profiles (2.2σ). The emission is red-shifted with a centroid velocity of 4.5 ± 1.0 km s^{-1}, similar to the red-shifted profiles of the confirmed He I detections in this work. The FWHM (23.5 ± 0.6 km s^{-1}) also agrees with those of the other He I lines in Table 1.

Appendix C: Disentangling He I λ3890 from H8

Fig. C.1 illustrates the He I λ3890 emission after Balmer emission at 3890.16 Å (H8) was modelled and subtracted from the spectrum. H8 emission has a wide, asymmetric profile spanning ~200 km s^{-1} on each wing. The least-χ^2 fit to its profile yields an NC (FWHM= 66 km s^{-1}) at −8.2 km s^{-1} and a BC (FWHM= 165 km s^{-1}) at 3.3 km s^{-1}. The composite fit to H8 was then subtracted from the spectrum, revealing the He I emission at 3889.75 Å.

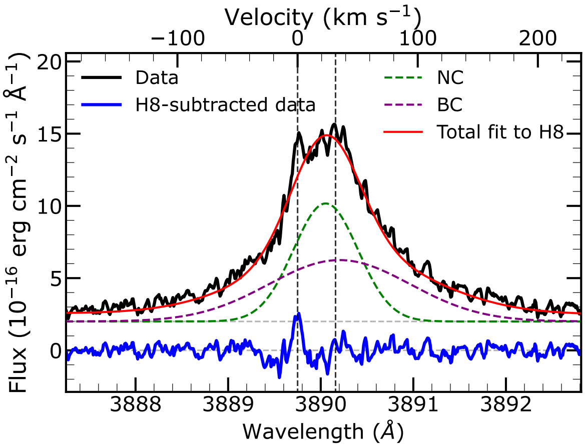

Fig. C.1. Least-χ^2 fit (red) to H8 in the spectrum (black) composed of NC (green) and BC (purple), plotted with a vertical offset of 2×10^{-16} erg s^{-1} cm^{-2} Å^{-1}. The data after subtracting this composite fit is shown in blue, revealing the He I emission at 3889.75 Å.

Appendix D: Evolution of NC and BC from class A to class C profiles

The NC and BC profiles of the asymmetric He I lines in the Delorme 1 (AB)b spectra show an increasing trend in intensities and widths from class A to class C. This is illustrated in Fig. D.1 for the triplet He I λ5877 and the singlet He I λ4923. The BC in the He I λ4923 profile is broader and more redshifted in class C epochs. Fig. D.2 shows the variation in the BC/NC flux ratio of the He I $\lambda\lambda$5877, 4923, 4473 line profiles from epoch to epoch. The line profiles of He I λ4923 and λ4473 vary from BC-dominated (BC/NC>1) to NC-dominated (BC/NC<1). He I λ5877 line profile remains mostly NC-dominated except on 13 October 2022.

Appendix E: Line flux from individual epochs

Table E.1 lists the integrated flux of He I lines detected from Delorme 1 (AB)b in this work from the median spectra from each observation night. Fig E.1 compares the variation of Hα and He I λ5877 emission lines from both the target and its primary with time. As evident from the plots, the primary shows very little variation compared to the companion, as is expected from chromospheric activity, except likely during a flare on 2 January 2023. The emission profile from the primary also lacks any asymmetry unlike in the companion spectra. Fig E.2 shows the line profile of He I λ5877 from the median of each night of observation, along with the respective NC and BC from the least-χ^2 fit to the profile. The characteristics of the respective profile fits from each night is given in Table E.2.

Appendix F: $L_{\rm acc}$ and $\dot{M}_{\rm acc}$ measurements from different accretion proxies

Table F.1 shows the $L_{\rm acc}$ and $\dot{M}_{\rm acc}$ measurements for the target obtained from UV excess using hydrogen slab models ENTROPY II and using Hα line luminosity and He I line luminosities based on $L_{\rm line}$–$L_{\rm acc}$ scaling relations. For the latter, we use both the Fiorellino et al. (2025) empirical scaling relations based on low-mass stars, as well as the Aoyama et al. (2021) planetary scaling relations developed based on shock emission models.

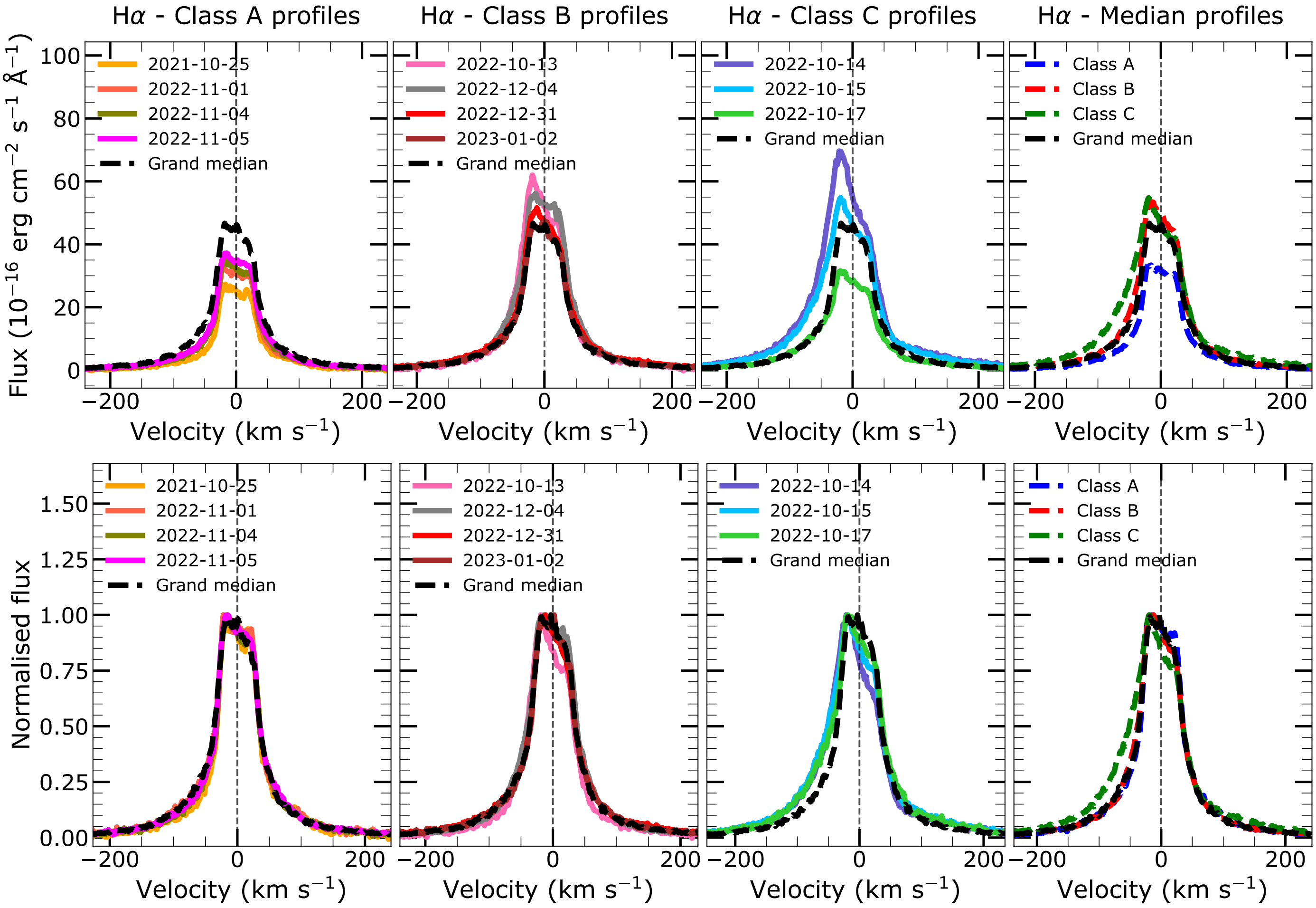

Fig. A.1. Class A, class B, and class C profiles of the Hα emission of Delorme 1 (AB)b. Right panels show the respective median profiles along with the grand median profile. Top panels illustrate the flux variation between individual epochs (in units of 10^{-16} erg cm^{-2} s^{-1} Å^{-1}) and bottom panels (with flux normalised to Hα peak intensity in the y-axis) demonstrate the comparison of profile shapes between the three classes.

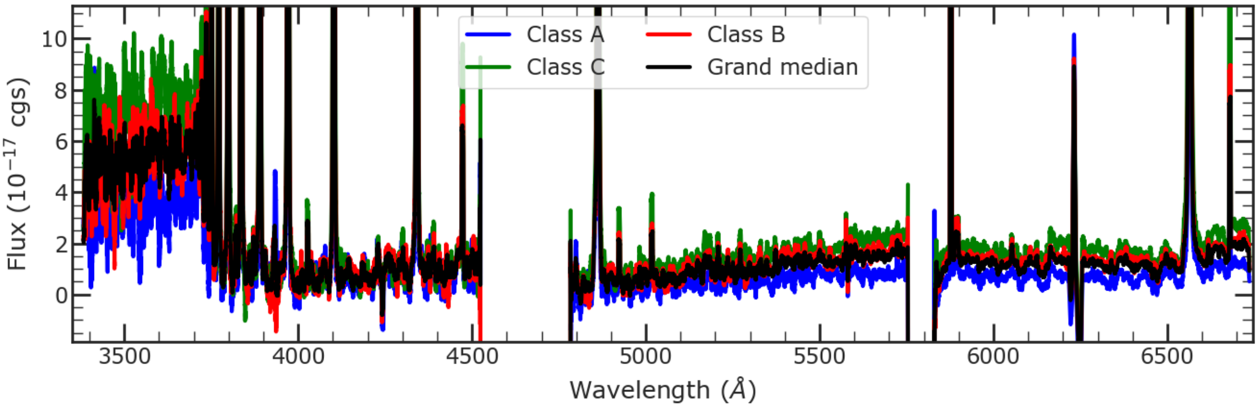

Fig. A.2. UVES spectrum of Delorme 1 (AB)b over the whole wavelength range, smoothened with a box size of 500 pixels. The rise in the UV excess and continuum level beyond ~5300 Å can be clearly seen in the class C median compared to class A and class B. ‘cgs’ denotes erg s^{-1} cm^{-2} Å^{-1}.

Table E.1. Integrated line fluxes for He I lines from individual nights, in units of 10^{-17} erg s^{-1} cm^{-2}.

Epoch	λ3890	λ4027	λ4473	λ4923	λ5017	λ5877	λ6680
2021-10-25	1.3 ± 8.4[a]	5.7 ± 8.9[a]	12.2 ± 9.5[a]	5.8 ± 4.7[a]	3.6 ± 4.2[a]	40.4 ± 1.9	13.6 ± 2.9
2022-10-13	1.6 ± 14.0[a]	6.2 ± 11.8[a]	10.1 ± 14.3	5.7 ± 7.3[a]	5.2 ± 6.8	60.6 ± 3.7	24.4 ± 4.3
2022-10-14	5.9 ± 9.2	17.1 ± 7.3	39.1 ± 8.8	12.1 ± 3.7	5.2 ± 3.8	116.2 ± 2.5	54.6 ± 5.3
2022-10-15	7.0 ± 6.5	13.3 ± 5.0	31.2 ± 6.2	10.7 ± 3.1	13.4 ± 3.8	101.1 ± 2.0	46.8 ± 2.8
2022-10-17	3.0 ± 7.0	9.8 ± 5.6	23.4 ± 7.2	7.1 ± 3.8	6.6 ± 3.2	66.7 ± 2.0	28.2 ± 2.3
2022-11-01	4.1 ± 10.5	3.8 ± 8.4[a]	18.5 ± 9.4	7.5 ± 4.4	3.7 ± 4.6	56.4 ± 3.2	23.2 ± 8.9
2022-11-04	3.8 ± 6.9	7.6 ± 5.7[a]	20.0 ± 7.1	4.6 ± 4.1	4.1 ± 3.8	58.9 ± 2.1	22.3 ± 2.1
2022-11-05	4.3 ± 7.3	3.7 ± 4.6	16.5 ± 8.0	6.9 ± 3.7	4.9 ± 3.4	63.6 ± 2.3	25.5 ± 2.3
2022-12-04	7.9 ± 6.0	11.6 ± 6.0	27.1 ± 7.2	4.1 ± 3.8	7.4 ± 3.0	88.7 ± 1.9	35.2 ± 2.1
2022-12-31	9.6 ± 8.4	9.6 ± 6.4	27.3 ± 7.8	8.6 ± 3.6	8.2 ± 3.7	87.7 ± 1.3	36.8 ± 2.2
2023-01-02	7.8 ± 9.1	7.9 ± 7.2	24.6 ± 9.4	10.2 ± 4.6	7.9 ± 5.6	84.1 ± 2.3	33.3 ± 2.4

Notes.

(a) Tentative Detections with S/N $1 - 3\sigma$, where σ denotes the standard deviation of the flux within ±150 km s^{-1}.

(b) Error bars on the flux values indicate the rms of the local continuum for each night.

Table E.2. Centroid velocities and FWHM, in units of km s^{-1}, of NC and BC from the least-χ^2 fit to the He I λ5877 emission line profile from each observation night.

Epoch	$\mu_{\rm NC}$	FWHM$_{\rm NC}$	$\mu_{\rm BC}$	FWHM$_{\rm BC}$	Flux$_{\rm BC}$/Flux$_{\rm NC}$
2021-10-25	0.4 ± 0.1	15.8 ± 0.2	18.1 ± 0.3	15.6 ± 0.6	0.37
2022-10-13	−0.5 ± 0.1	14.3 ± 0.5	10.8 ± 0.8	28.0 ± 0.8	1.65
2022-10-14	−1.1 ± 0.1	16.3 ± 0.2	15.1 ± 0.4	22.1 ± 0.5	0.76
2022-10-15	−0.6 ± 0.1	16.5 ± 0.2	15.6 ± 0.5	22.2 ± 0.6	0.71
2022-10-17	1.0 ± 0.1	17.0 ± 0.2	19.0 ± 0.3	18.4 ± 0.4	0.45
2022-11-01	1.6 ± 0.1	17.6 ± 0.2	20.0 ± 0.1	15.6 ± 0.6	0.31
2022-11-04	0.4 ± 0.1	15.3 ± 0.2	16.5 ± 0.5	21.6 ± 0.8	0.57
2022-11-05	−0.6 ± 0.1	15.4 ± 0.2	14.7 ± 0.8	25.2 ± 1.0	0.73
2022-12-04	0.6 ± 0.1	16.5 ± 0.2	17.0 ± 0.5	21.6 ± 0.8	0.53
2022-12-31	0.1 ± 0.2	16.8 ± 0.2	16.6 ± 0.5	21.1 ± 0.7	0.60
2023-01-02	0.1 ± 0.1	16.2 ± 0.2	17.5 ± 0.3	19.4 ± 0.5	0.49

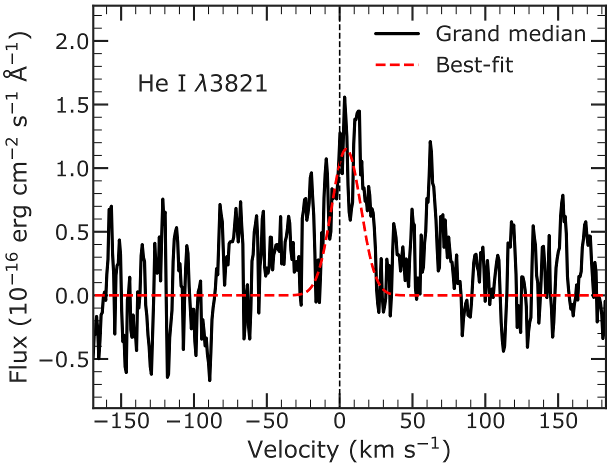

Fig. B.1. Tentative detection of He I λ3821 emission in the grand median UVES spectrum of Delorme 1 (AB)b. The least-χ^2 fit to the line profile is shown in red.

Table F.1. $L_{\rm acc}$ and $\dot{M}_{\rm acc}$ measured from Delorme 1 (AB)b using different parameters.

Epoch	Measured from	$\log(L_{\rm acc}/L_\odot)$	$\dot{M}_{\rm acc}$ ($M_\odot$yr^{-1})
UVES	UV excess	$-5.3^{+0.5}_{-0.4}$	$1-3\times10^{-12}$
UVES	He I (FAM25)	$-4.9^{+0.3}_{-0.3}$	7.4×10^{-12}
UVES	Hα (FAM25)	$-5.5^{+0.4}_{-0.2}$	1.4×10^{-12}
UVES	Hα (AMI21)	$-4.3^{+0.3}_{-0.2}$	2.6×10^{-11}
MUSE	Hα (FAM25)	$-6.6^{+0.4}_{-0.2}$	1.3×10^{-13}

Notes.
FAM25 and AMI21 denotes $L_{\rm line}$–$L_{\rm acc}$ scaling relations from Fiorellino et al. (2025) and Aoyama et al. (2021) respectively. The uncertainties indicated on the $L_{\rm acc}$ measurements are based on the lowest and highest values over the observations epochs.

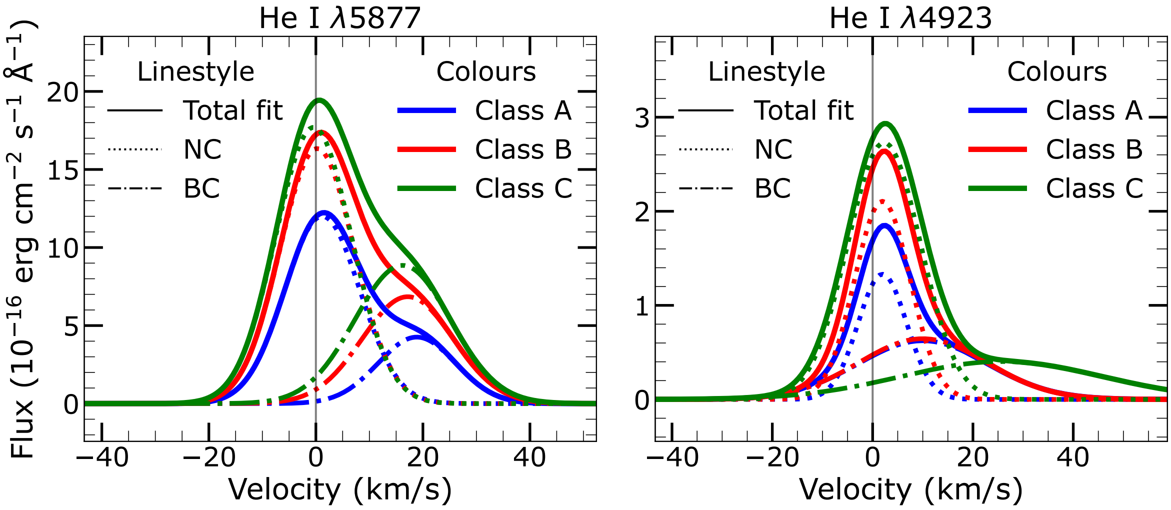

Fig. D.1. Decomposition into NC and BC for the median profiles of the He I lines λ5877 and λ4923 from class A, class B, and class C epochs of Delorme 1 (AB)b. The line-styles represent the NC (dotted), BC (dashed) and total fits (solid) to the profiles, while the colours represent the median class A (blue), class B (red) and class C (green) epochs.

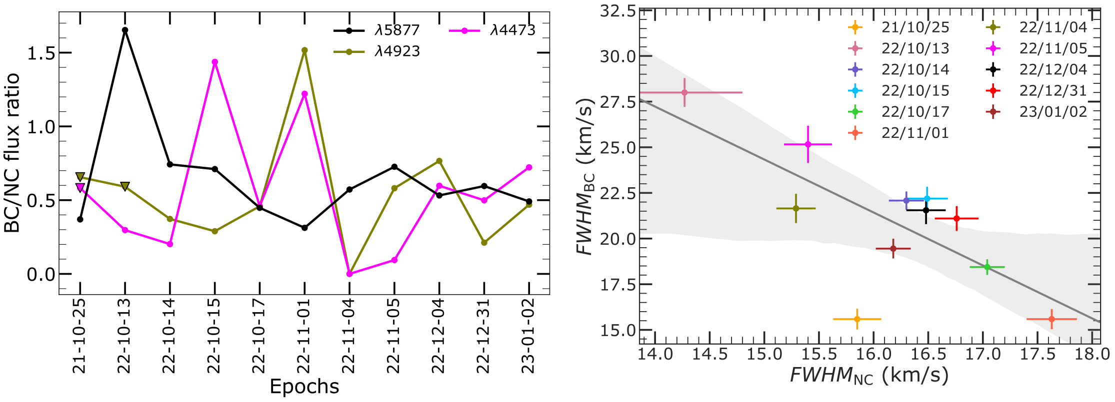

Fig. D.2. (Left) Variation in the BC/NC flux ratio of He I λλ5877, 4923, 4473 emission lines with time. He I λ4027 is not shown in the figure since it is of much lower S/N with its profiles from individual nights relatively noisy. (Right) Variation in the FWHM of NC and BC through the epochs for He I D3 line. The widths of both the components are anti-correlated (grey line and shaded region denotes the linear fit and its uncertainty), with the overall profile shape remaining the same with time.

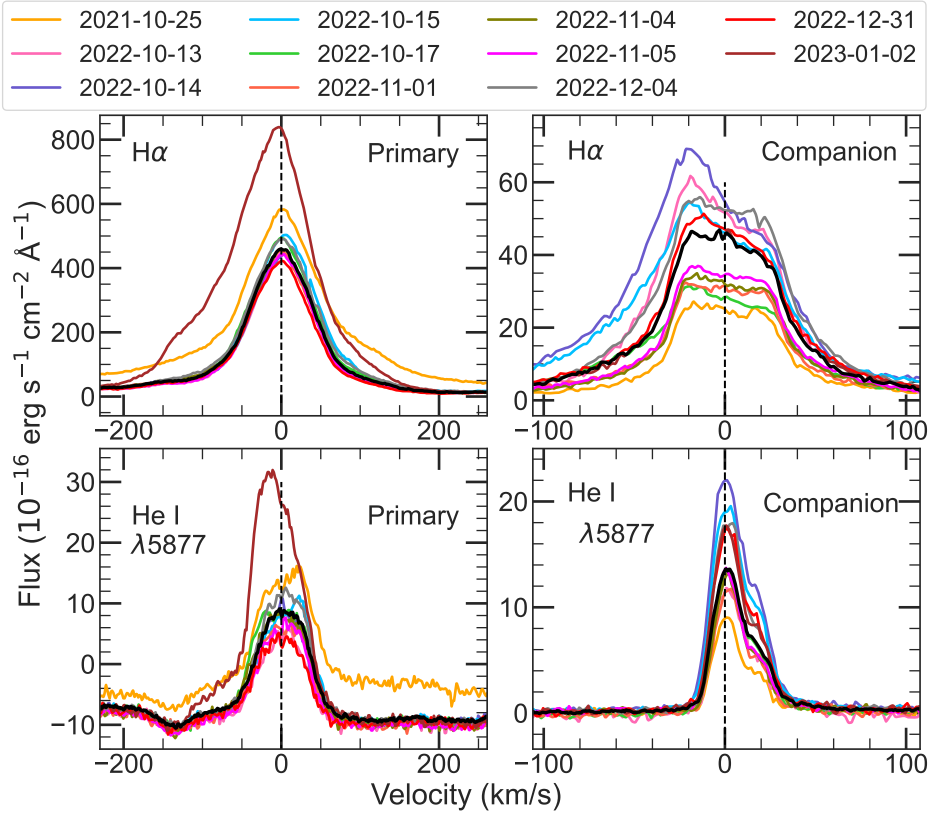

Fig. E.1. Hα (top panel) and He I λ5877 (bottom panel) emission lines detected from the primary (left) and the companion (right) during each observation night. The grand median profile is represented by a thick black curve in each panel.

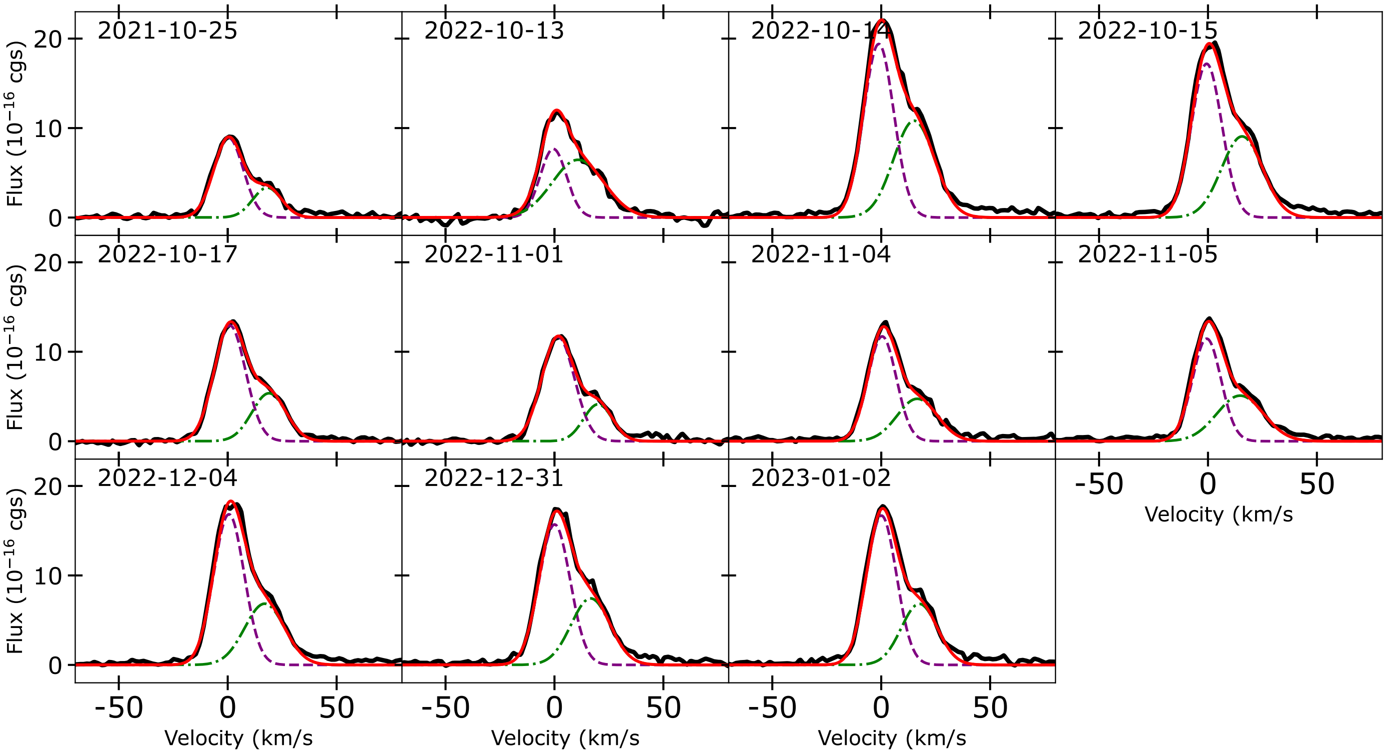

Fig. E.2. He I λ5877 emission from the median of each night of observation, with the respective least-χ^2 fit to its profile. Colours and symbols hold the same meaning as in Fig. 1. cgs stands for erg s^{-1} cm^{-2} Å^{-1}.